

# Earth and Space Science

## RESEARCH ARTICLE

10.1029/2024EA004165

### Special Collection:

TEMPO Data Products, Science, and Applications

### Key Points:

- TEMPO cloud product supports TEMPO trace gas retrievals
- Effective cloud fraction is derived at 466 nm and optical centroid pressure exploits the O<sub>2</sub>-O<sub>2</sub> spectral feature near 477 nm
- Sensitivities of the results to input variables are examined

### Supporting Information:

Supporting Information may be found in the online version of this article.

### Correspondence to:

H. Wang,  
hwang@cfa.harvard.edu

### Citation:

Wang, H., Nowlan, C. R., González Abad, G., Chong, H., Hou, W., Houck, J. C., et al. (2025). Algorithm theoretical basis for Version 3 TEMPO O<sub>2</sub>-O<sub>2</sub> cloud product. *Earth and Space Science*, 12, e2024EA004165. <https://doi.org/10.1029/2024EA004165>

Received 19 DEC 2024

Accepted 29 DEC 2024

### Author Contributions:

**Conceptualization:** Huiqun Wang,

Xiong Liu, Kelly Chance

**Data curation:** Huiqun Wang, Caroline R. Nowlan, Gonzalo González Abad, Heesung Chong, Weizhen Hou, John C. Houck

**Formal analysis:** Huiqun Wang

**Funding acquisition:** Xiong Liu, Kelly Chance

**Investigation:** Huiqun Wang













**Methodology:** Huiqun Wang, Eun-Su Yang, Alexander Vasilkov, Joanna Joiner

**Project administration:** Xiong Liu

© 2025. The Author(s).

This is an open access article under the terms of the [Creative Commons Attribution-NonCommercial-NoDerivs License](#), which permits use and distribution in any medium, provided the original work is properly cited, the use is non-commercial and no modifications or adaptations are made.

## Algorithm Theoretical Basis for Version 3 TEMPO O<sub>2</sub>-O<sub>2</sub> Cloud Product

Huiqun Wang<sup>1</sup> , Caroline R. Nowlan<sup>1</sup> , Gonzalo González Abad<sup>1</sup> , Heesung Chong<sup>1</sup>, Weizhen Hou<sup>1</sup>, John C. Houck<sup>1</sup> , Xiong Liu<sup>1</sup> , Kelly Chance<sup>1</sup> , Eun-Su Yang<sup>2</sup>, Alexander Vasilkov<sup>2</sup>, Joanna Joiner<sup>3</sup> , Wenhan Qin<sup>2</sup>, Zachary Fasnacht<sup>2</sup> , K. Emma Knowland<sup>3,4</sup> , Chris Chan Miller<sup>1,5,6</sup>, Robert J. D. Spurr<sup>7</sup> , David E. Flittner<sup>8</sup>, James L. Carr<sup>9</sup> , Raid M. Suleiman<sup>1</sup> , John E. Davis<sup>1</sup>, and Jean A. Fitzmaurice<sup>1</sup>

<sup>1</sup>Smithsonian Astrophysical Observatory (SAO), Cambridge, MA, USA, <sup>2</sup>Science Systems and Applications, Inc. (SSAI), Lanham, MD, USA, <sup>3</sup>NASA Goddard Space Flight Center (GSFC), Greenbelt, MD, USA, <sup>4</sup>Morgan State University, Baltimore, MD, USA, <sup>5</sup>Harvard University, Cambridge, MA, USA, <sup>6</sup>Environmental Defense Fund, New York, NY, USA, <sup>7</sup>RT Solutions Inc., Cambridge, MA, USA, <sup>8</sup>NASA Langley Research Center, Hampton, VA, USA, <sup>9</sup>Carr Astronautics Corporation, Washington, DC, USA

**Abstract** This Algorithm Theoretical Basis Document (ATBD) describes the retrieval algorithm and sensitivities of the Version 3 cloud product derived from the spectra collected by the Tropospheric Emissions: Monitoring of POLLution (TEMPO) instrument. The cloud product is primarily produced for supporting the retrievals of TEMPO trace gases that are important for understanding atmospheric chemistry and monitoring air pollution. The TEMPO cloud algorithm is adapted from NASA's Ozone Monitoring Instrument (OMI) oxygen collision complex (O<sub>2</sub>-O<sub>2</sub>) cloud algorithm. The retrieval generates effective cloud fraction (ECF) from the normalized radiance at 466 nm and generates cloud optical centroid pressure (OCP) using the O<sub>2</sub>-O<sub>2</sub> column amount derived from the spectral absorption feature near 477 nm. The slant column of O<sub>2</sub>-O<sub>2</sub> is retrieved using Smithsonian Astrophysical Observatory's spectral fitting code with optimized retrieval parameters. ECF and OCP are used by TEMPO trace gas retrievals to calculate Air Mass Factors which convert slant columns to vertical columns. The sensitivities of the cloud retrieval to various input parameters are investigated.

**Plain Language Summary** This Algorithm Theoretical Basis Document describes the retrieval algorithm and characteristics of the Version 3 cloud product for the Tropospheric Emissions: Monitoring of POLLution (TEMPO) instrument. The product provides cloud fraction and cloud pressure information to support retrievals of TEMPO trace gases, such as nitrogen dioxide and formaldehyde, which are important indicators of air pollution. Sensitivity studies are performed to assess the changes in cloud information with respect to various input parameters.

## 1. Introduction

### 1.1. TEMPO Overview

Tropospheric Emissions: Monitoring of POLLution (TEMPO) (Zoogman et al., 2017) is NASA's first Earth Venture Instrument (EVI-1) project. TEMPO was launched on 7 April 2023 on board the commercial geostationary communication satellite IntelSat-40e (IS- 40e) via a SpaceX Falcon 9 rocket into a geostationary orbit parked at 91°W. TEMPO has been operating since first light (1 August 2023 for irradiance and 2 August for radiance).

TEMPO uses Ultraviolet (UV)/visible spectroscopic techniques to monitor atmospheric pollution across North America hourly at several kilometers scale resolution (Figure 1). TEMPO measures spectra required to retrieve a suite of trace gases and parameters, such as columns of ozone (O<sub>3</sub>), nitrogen dioxide (NO<sub>2</sub>), sulfur dioxide (SO<sub>2</sub>), formaldehyde (HCHO), glyoxal (C<sub>2</sub>H<sub>2</sub>O<sub>2</sub>), water vapor (H<sub>2</sub>O), aerosols, cloud parameters, and Ultraviolet B (UVB) radiation.

TEMPO measurements capture the inherent high variability in the diurnal cycle of emissions and chemistry. Pollution sources can be resolved at a sub-urban scale on an hourly basis. The fine temporal and spatial resolution can advance current understanding of atmospheric chemistry and transport, improve emission estimates, and better monitor population's exposure to pollutants.

**Resources:** Xiong Liu, Wenhan Qin, Zachary Fasnacht, K. Emma Knowland, Chris Chan Miller, Robert J. D. Spurr, David E. Flittner, James L. Carr, Raid M. Suleiman, John E. Davis, Jean A. Fitzmaurice  
**Software:** Huiqun Wang, Caroline R. Nowlan, Gonzalo González Abad, Heesung Chong, Weizhen Hou, John C. Houck, Eun-Su Yang, Alexander Vasilkov, Joanna Joiner  
**Supervision:** Xiong Liu  
**Validation:** Huiqun Wang, Caroline R. Nowlan, Gonzalo González Abad  
**Visualization:** Huiqun Wang  
**Writing – original draft:** Huiqun Wang, Caroline R. Nowlan, Gonzalo González Abad  
**Writing – review & editing:** Huiqun Wang, Caroline R. Nowlan, Gonzalo González Abad, Heesung Chong, Weizhen Hou, Eun-Su Yang, Alexander Vasilkov, Joanna Joiner, Wenhan Qin

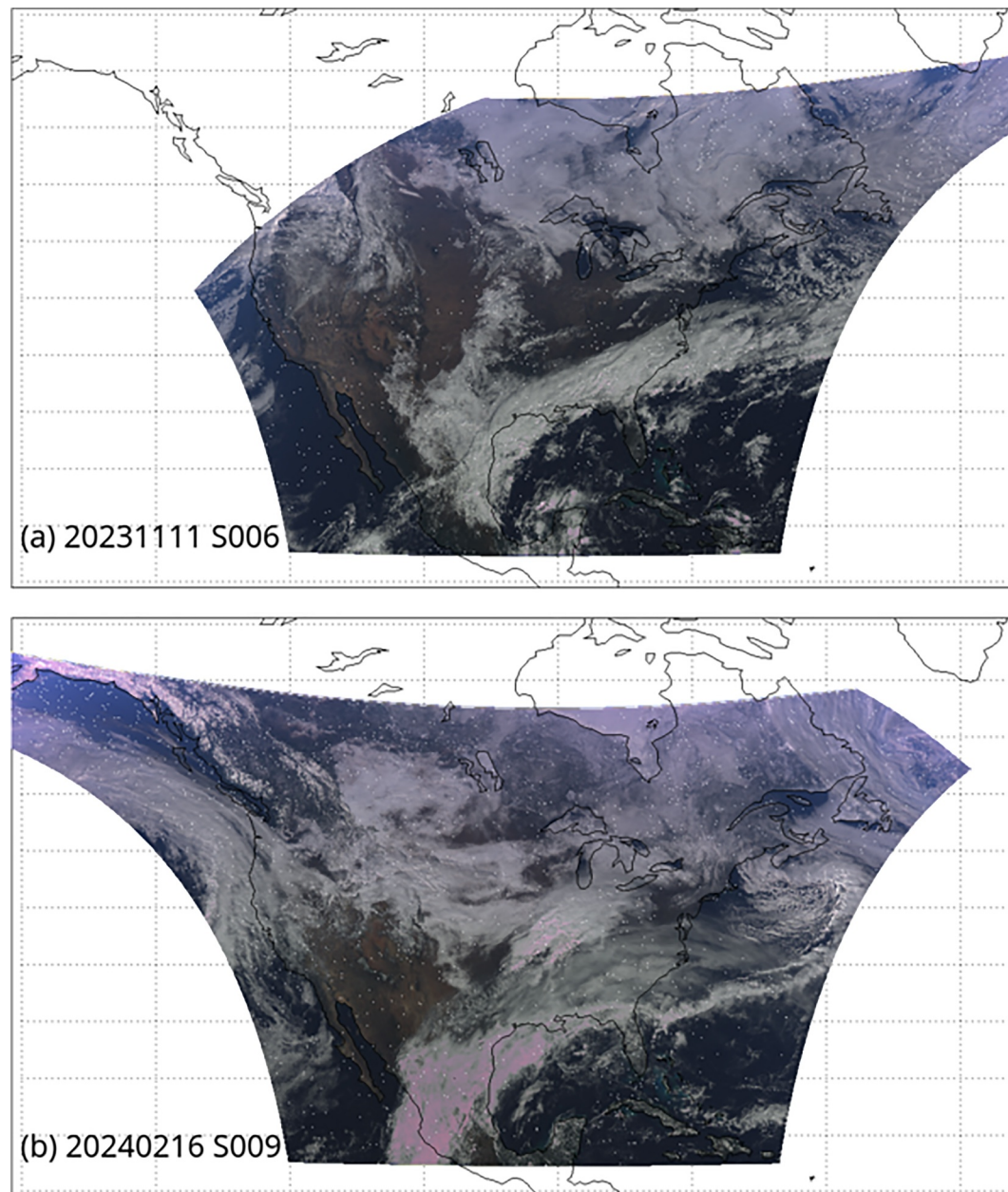


**Figure 1.** TEMPO true color image for Scan (a) S006 on 11 November 2023 and (b) S009 on 16 February 2024. Each scan starts from the east and continues toward the west. The pinkish colored clouds in Panel (b) suggest potential spectral saturation in blue. Areas outside TEMPO's field of regard or with solar zenith angle SZA > 80° are omitted.

## 1.2. TEMPO Instrument and Measurements

The TEMPO instrument is a UV/visible imaging grating spectrometer using 2 two-dimensional (spatial vs. spectral) Charge-Coupled Device (CCD) detectors in one focal plane covering UV band (293–494 nm) and visible band (538–741 nm). The TEMPO instrument slit aligns in the North-to-South direction and simultaneously measures 2,048 cross-track spatial pixels (with the 1st spatial pixel starting from the north). Each band has 1,028 spectral pixels. The spectral resolution is about 0.6 nm at Full Width at Half Maximum (FWHM) and the spectral sampling is about 0.2 nm. The TEMPO pixel area on the ground depends on the viewing geometry. At the center of the field of regard, the pixel resolution is about  $2.0 \times 4.75 \text{ km}^2$ . The TEMPO Level 0-1 ATBD (Chong et al., 2025) describes the instrument and measurement details.

TEMPO can make three types of measurements: Earth view radiance, solar irradiance, and dark current measurements. The calibration mechanism assembly controls the instrument aperture via a wheel with four selectable positions (open, closed, working diffuser, reference diffuser). The two diffusers record the Top-Of-Atmosphere (TOA) solar irradiance. The working diffuser is used for providing trace gas retrieval's solar spectrum on a time scale of days. The reference diffuser is used every few months for trending the degradation of the working diffuser.

Under nominal Earth view operation, TEMPO scans the field of regard from the east to the west each hour. Figure 1 shows the color images for two nominal TEMPO scans obtained on different dates. These images are composed using the “red” (R), “green” (G), and “blue” (B) variables in the “cloud\_mask” group of the TEMPO Level 1B (L1B) data product which mimics the true colors (Chong et al., 2025). The values of the R, G, and B variables are each stretched to the 0–255 range from the 0.0 to 1.0 range before they are combined into the color images.

In the early morning and late afternoon, TEMPO can operate in an optimized scan mode, measuring the daylight portion of the field of regard more frequently. In addition, TEMPO can use up to 25% of the observation time to perform special observations where a selected portion of the TEMPO field of regard is scanned at higher temporal resolution (e.g., minutes).

TEMPO data for each day are organized according to scan numbers (e.g., S001 denotes the 1st scan of each day). To keep the file size manageable, TEMPO data for each scan are split into multiple granules, with each granule covering the observations obtained within a few minutes.

## 2. Context

### 2.1. Historical Perspective

TEMPO makes the first tropospheric trace gas measurements from a geostationary (GEO) orbit for North America by building upon the heritage of previous spectrometers (e.g., Global Ozone Monitoring Experiment (GOME), Scanning Imaging Absorption Spectrometer for Atmospheric Cartography (SCIAMACHY), Ozone Monitoring Instrument (OMI), Global Ozone Monitoring Experiment-2 (GOME-2), Ozone Mapping and Profiler Suite (OMPS) and TROPOspheric Monitoring Instrument (TROPOMI)) in low-earth-orbit (LEO) (Bovensmann et al., 1999; Burrows et al., 1999; Flynn et al., 2014; Levelt et al., 2006; Munro et al., 2016; Veefkind et al., 2012). Novel to TEMPO are hourly measurements with finer spatial resolution. The observational strategy makes TEMPO an innovative application of well-proven techniques, contributing to air quality and climate applications.

The TEMPO cloud product CLDO4 is primarily used for supporting the TEMPO trace gases (e.g., NO<sub>2</sub>, HCHO). The cloud retrieval uses the same TEMPO spectra, reference spectra, slant column fitting code, ancillary surface and meteorological inputs as those used by the TEMPO trace gas retrievals. The TEMPO CLDO4 code is based on Smithsonian Astrophysical Observatory (SAO)'s spectral fitting algorithm (González Abad et al., 2015) and NASA Goddard Space Flight Center (GSFC)'s OMI O<sub>2</sub>-O<sub>2</sub> cloud algorithm for the OMCDO4 product (Vasilkov et al., 2018). This paper describes the details of the retrieval algorithm run at SAO's Science Data Processing Center (SDPC) to generate the Version 3 TEMPO CLDO4 product.

### 2.2. Additional Information

The Version 3 Level 2 (L2) and Level 3 (L3) TEMPO data for the May 2024 public release are processed using the Version 4.4 SDPC pipeline. The software version and data version can be found in the global attributes of each TEMPO product file. A user guide accompanies the data release and provides additional information on the data format and usage recommendations. Supporting Information S1 for this paper provide details on the input/output variables and acronyms/symbols.

TEMPO data are available through NASA Earthdata ([earthdata.nasa.gov](https://earthdata.nasa.gov)) Atmospheric Science Data Center (ASDC, [asdc.larc.nasa.gov](https://asdc.larc.nasa.gov)). Quick view for the L2 and L3 TEMPO CLDO4, NO<sub>2</sub>, HCHO and other products is available through NASA Worldview website ([worldview.earthdata.nasa.gov](https://worldview.earthdata.nasa.gov)).

### 3. Algorithm Description

#### 3.1. Background

The TEMPO CLDO4 product contains cloud fraction and cloud pressure that are required for calculating Air Mass Factors (AMFs) for TEMPO trace gases, as well as for filtering retrievals with various degrees of cloud contamination. Air Mass Factors (Martin et al., 2002; Palmer et al., 2001) convert slant column densities (SCDs) obtained from spectral fitting to vertical column densities (VCDs,  $VCD = SCD/AMF$ ) of trace gases. An AMF quantifies the light path from the sun to the surface and back to the detector. It depends on surface reflectance properties, vertical profiles of absorbers and scatterers in the atmosphere for the wavelengths of interest and geometry of illumination and observation.

Clouds greatly influence trace gas retrieval results through the AMFs. As an example, a conservative estimate of the total uncertainty in tropospheric AMF for  $NO_2$  is about 35%–60% for which the uncertainty in cloud parameters is amongst the leading errors (Boersma et al., 2004; Lorente et al., 2017).

The complexity of cloud effects on the radiation field requires simplifications for efficient trace gas retrievals when data volume is large. Thus, clouds within each scene are often assumed to be homogeneous and suitable for the Independent Pixel Approximation (IPA) (Zuidema & Evans, 1998), where a pixel is modeled as composed of a clear part and an overcast part. Using radiative transfer modeling under typical conditions encountered by OMI, Stammes et al. (2008) found that Rayleigh scattering and gaseous absorption can be well modeled when clouds are approximated as Lambertian surfaces with reflectance  $R_c = 0.8$ –0.9 within a model known as the mixed Lambertian-equivalent reflectivity (MLER). With these  $R_c$  values, the consistently derived cloud pressure lies at a height well below the geometric or thermal cloud top and the results of trace gas retrievals are optimized (Joiner et al., 2012; Sneep et al., 2008; Stammes et al., 2008; Vasilkov et al., 2004, 2008; Veeffkind et al., 2016).

The TEMPO CLDO4 algorithm derives Effective Cloud Fraction (ECF) and cloud Optical Centroid Pressure (OCP) assuming  $R_c = 0.8$  following the heritage from OMI. Cloud reflectance varies with cloud optical depth  $\tau$  among other factors, such as microphysics, phase, morphology, and geometry (Gatebe & King, 2016). There is a rapid increase of  $R_c$  with  $\tau$  when  $\tau < 30$  and a slower increase for larger  $\tau$  values (Chang et al., 2000). Using the Earth Radiation Budget Experiment (ERBE) observations, Chang et al. (2000) showed that cloud reflectance is typically  $< 0.7$  for the short wave (0.2–5  $\mu m$ ) band and can approach 0.8 when  $\tau > 100$ . Consequently, the fixed cloud albedo of  $R_c = 0.8$  implies a very large  $\tau$ , other factors being equal.

Cloud fraction and cloud pressure are dependent upon the spatial resolution, wavelength, cloud type, morphology, and even illumination—observation geometry (Kobayashi, 1993; Sneep et al., 2008). Consequently, the retrieved cloud parameters are “effective” values that are specific to the condition for each pixel, and they are not necessarily equivalent to the cloud information observed by other instruments even at the same moment in time.

Cloud retrieval requires ancillary information on surface reflectance, surface pressure, specific humidity ( $Q$ ) and temperature ( $T$ ) versus pressure ( $p$ ) profiles, all of which are also required by trace gas AMFs. Changes in a priori inputs translate into direct changes in both the cloud information and the clear-sky part of trace gas AMF, as well as into indirect changes in the cloudy part of trace gas AMF through cloud information. Consistency between clouds and trace gas AMFs offers the possibility that some of the biases in ancillary data may cancel out for cloudy scenes, though others may amplify. Lorente et al. (2017) found that structural uncertainty associated with different cloud correction approaches can result in substantial (5%–40%) differences for trace gas AMFs under polluted conditions for low cloud fractions  $< 0.2$ .

#### 3.2. Theory

##### 3.2.1. Theoretical Basis for Cloud Retrieval

The measured TOA sun normalized radiance ( $I_m$ ) is assumed to be the sum of a clear-sky ( $I_g$ ) and an overcast ( $I_c$ ) part weighted by an effective cloud fraction (ECF, also denoted as  $f$  in Equation 1 (Vasilkov et al., 2018)).  $I_g$  and  $I_c$  for each scene geometry are obtained from a pre-computed Look-Up-Table (LUT) using the Lambertian equivalent reflectivity (LER) for ground ( $R_g$ ) and cloud ( $R_c$ ), respectively. Effective cloud fraction is calculated as  $f = (I_m - I_g)/(I_c - I_g)$ .

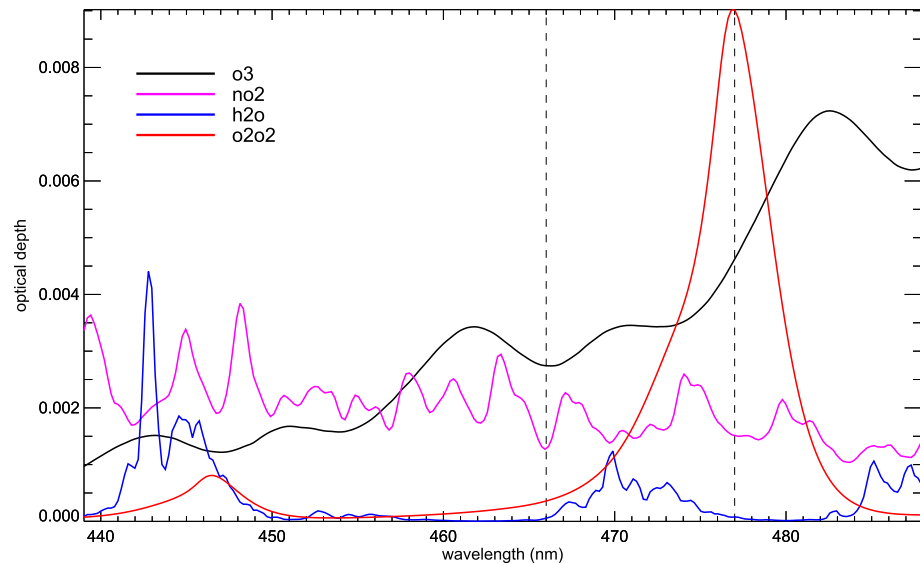


**Figure 2.** Typical optical depths of trace gases as a function of wavelengths within the 439–488 nm O<sub>2</sub>-O<sub>2</sub> fitting window. Different colors represent different molecules. Molecular spectra are convolved with the TEMPO slit function. Molecular abundance used are 325 DU of O<sub>3</sub>, 1.3e + 43 molecules<sup>2</sup> cm<sup>-5</sup> of O<sub>2</sub>-O<sub>2</sub>, 1.0e + 23 molecules cm<sup>-2</sup> (i.e., 29.89 mm) of H<sub>2</sub>O, and 5.0e + 15 molecules cm<sup>-2</sup> of NO<sub>2</sub>. Dashed lines indicate 466 and 477 nm.

$$I_m = I_g \cdot (1 - f) + I_c \cdot f \quad (1)$$

The TEMPO cloud algorithm is originally adapted from the NASA's OMI O<sub>2</sub>-O<sub>2</sub> cloud algorithm (Vasilkov et al., 2018). The ECF is derived from the sun normalized TOA radiance (i.e., radiance/irradiance) at 466 nm. This wavelength is chosen because it is not significantly affected by trace gas absorption and because it is close to the 477 nm region where the O<sub>2</sub>-O<sub>2</sub> spectral feature is used to derive cloud pressure (Figure 2). It is worth noting that ECF relies on the radiance to irradiance ratio at a single wavelength, making it especially sensitive to the absolute calibration of the LIB spectrum. In comparison, the O<sub>2</sub>-O<sub>2</sub> spectral fitting is more tolerable to uncertainties in radiance and irradiance calibration as the closure polynomials in the fitting algorithm can account for some calibration error of radiance and irradiance.

Consistent with the TEMPO trace gas algorithms, TEMPO clouds are represented as Lambertian reflectors with  $R_c = 0.8$  following the approach used in the OMI cloud algorithms (Vasilkov et al., 2018). It should be noted that the retrieved ECF depends on the assumed  $R_c$ . Had  $R_c = 0.9$  (Stammes et al., 2008) been used, the retrieved cloud fractions over typical surfaces would be expected to be smaller, as a smaller fraction of brighter clouds is needed to match the measured radiance.

To account for the effect of surface Bi-directional Reflectance Distribution Function (BRDF) on radiative transfer, our algorithms employ the Geometry-dependent Lambertian Equivalent Reflectivity (GLER) concept (Fasnacht et al., 2019; Qin et al., 2019; Vasilkov et al., 2017). Using this approach, the LUTs (Section 3.4) prepared for Lambertian surfaces can be directly used for the CLDO4 retrieval (Vasilkov et al., 2017).

Aerosols are not explicitly treated in the TEMPO cloud algorithm for Version 3 data and their influence is implicit in the retrieved cloud information (Qin et al., 2019; Vasilkov et al., 2018). For consistency, TEMPO trace gas AMFs use TEMPO cloud information without explicitly considering aerosols. In a case study on polluted conditions in northern China, Vasilkov et al. (2021) found that explicit treatment of aerosols in cloud algorithm can decrease the retrieved ECF by 0.01 and increase the retrieved cloud pressure by about 100 hPa for low-altitude clouds and about 50 hPa for mid-altitude clouds. For the TEMPO scans on 30 September 2023, thick smokes from wildfires are aliased as clouds with ECF values of ~0.5 or more, which implies that the Version 3 ECF data may lead to cloud misclassification on occasions.

The cloud optical centroid pressure (OCP, also denoted as  $P_c$ ) is derived from the O<sub>2</sub>-O<sub>2</sub> SCD using Equation 2, where VCD is the vertical column density. The clear-sky VCD( $P_s$ ) and overcast VCD( $P_c$ ) are calculated using surface pressure  $P_s$  and cloud optical centroid pressure  $P_c$ , respectively. The VCD calculations employ the vertical profiles of specific humidity ( $Q$ ) and temperature ( $T$ ) from the GEOS Composition Forecasting (GEOS-CF) product (typically available within 24-hr of TEMPO observation) (Knowland et al., 2022). Clear-sky AMF<sub>g</sub> and cloudy-sky AMF<sub>c</sub> at different pressures are obtained from a pre-computed AMF LUT at 477 nm. The cloud radiance fraction (CRF, also denoted as  $f_r = f * (I_c/I_m)$ ) represents the fraction of radiance reflected by clouds (see Equation 1).

In the V4.4 SDPC pipeline, CRF at 466 nm is used in the OCP retrieval. Although the O<sub>2</sub>-O<sub>2</sub> spectral feature exploited for OCP has peak absorption at 477 nm, the retrieval window spans 439–488 nm, and a few interfering molecules also absorb within the window. As the Lambertian cloud reflectance is fixed at 0.8, the spectral dependence of  $f_r$  associated with reflectance primarily comes from  $I_m$ . For large  $f$ ,  $I_c$  is close to  $I_m$ , and  $f_r$  is close to  $f$ . For small  $f$ , typically  $f_r > f$  as  $I_c$  is significantly larger than  $I_m$ , and a large portion of the spectral variation of  $I_m$  is due to surface reflectance, atmospheric Rayleigh scattering and aerosols, in addition to atmospheric absorption. As 466 nm is close to 477 nm at which the AMF LUT is constructed, CRF at 466 nm provides a reasonable approximation to CRF at 477 nm. We will implement GLER at 477 nm in future SDPC pipeline to enable the usage of CRF at 477 nm for OCP derivation. This will keep consistency with the AMF LUT. However, as the LUTs are constructed under a few assumptions, there are also errors associated with using the LUTs.

OCP is derived by iteratively adjusting  $P_c$  on the right-hand side of Equation 2 to match the SCD retrieved from spectral fitting on the left-hand side. Note that a change in ECF (i.e.,  $f$ ) and therefore  $f_r$  will lead to a change in  $P_c$  because the sum on the right-hand side of Equation 2 needs to match the retrieved SCD (Vasilkov et al., 2021). In other words, ECF and OCP work in pairs. The OCP retrieved using this model is usually located within a scattering cloud at a height below the geometrical cloud top (Joiner et al., 2012; Vasilkov et al., 2008), and there is a tendency for OCP to decrease with increasing geometric Air Mass Factor (AMF<sub>geo</sub> = 1/cos(Solar Zenith Angle) + 1/cos(Viewing Zenith Angle)), that is, OCP appears closer to the cloud top when geometric air mass factor is large (Sneep et al., 2008).

$$\text{SCD} = (1 - f_r) \cdot \text{AMF}_g(P_s, R_g) \cdot \text{VCD}(P_s) + f_r \cdot \text{AMF}_c(P_c, R_c) \cdot \text{VCD}(P_c) \quad (2)$$

For trace-gas retrievals, it is essential to estimate the photon path lengths in the atmosphere that determine trace-gas absorption and thus affect the measured TOA radiance. The cloud algorithm, based on the O<sub>2</sub>-O<sub>2</sub> absorption band (Vasilkov et al., 2018), is consistent with the trace-gas algorithms in the use of the MLER approach. The MLER model compensates for photon path within a cloud by placing the Lambertian surface somewhere in the middle of the cloud instead of at the top (Vasilkov et al., 2008). As clouds are vertically inhomogeneous, the pressure of this surface does not necessarily correspond to the geometrical center of the cloud, but rather to the so-called optical centroid (Joiner et al., 2012; Vasilkov et al., 2008). The OCP can be thought of and modeled as a reflectance-averaged pressure level reached by backscattered photons (Joiner et al., 2012). Cloud OCPs are appropriate to use in trace gas retrievals from UV-Visible satellite instruments (Joiner et al., 2009; Vasilkov et al., 2004). Cloud-top pressures derived from thermal infrared (IR) measurements (e.g., Moderate Resolution Imaging Spectroradiometer (MODIS), Visible Infrared Imaging Radiometer Suite (VIIRS)) are different from the OCPs and do not provide good estimates of solar photon path lengths through clouds that are needed for trace-gas retrievals (Joiner et al., 2012; Vasilkov et al., 2008).

As in Vasilkov et al. (2018), the cloud code also calculates a scene Lambertian Equivalent Reflectance  $R_{\text{scene}}$  and a scene pressure  $P_{\text{scene}}$  using Equations 3 and 4. When  $f = 1$ ,  $I_m = I_c$  (see Equation 1), thus  $f_r = 1$ . Equation 2 reduces to Equation 3 with  $R_c = R_{\text{scene}}$  and  $P_c = P_{\text{scene}}$ . Thus,  $R_{\text{scene}}$  can be considered as the LER of the scene assuming a full cloud cover at  $P_{\text{scene}}$ .

In Equation 4,  $I_{0b}$  is the TOA normalized radiance for a black surface,  $T_r$  is the total (direct + diffuse) normalized radiation reaching the surface converted to the ideal Lambertian reflected radiance (by dividing by  $\pi$ ) and then multiplied by the transmittance between the surface and TOA in the direction of the detector,  $S_b$  is the diffuse flux reflectivity of the atmosphere for the case of isotropic illumination from below (Vasilkov et al., 2018).  $I_{0b}$ ,  $T_r$ , and  $S_b$  are calculated for known surface pressure by solving three equations using the  $I_{\text{TOA}}$  values corresponding to LER values of 0.0, 0.1, and 0.2 in the pre-computed LUT at 477 nm (Qin et al., 2019). The results, in combination

with the measured  $I_{\text{TOA}}$  (i.e.,  $I_m$ ), are used to solve  $R_{\text{scene}}$  and  $P_{\text{scene}}$ . In theory,  $P_{\text{scene}} = P_s$  in the absence of clouds and aerosols, thus, it can be used as a consistency check to indicate potential problems with the cloud retrieval (Vasilkov et al., 2018). In V4.4 SDPC,  $P_{\text{scene}}$  and  $R_{\text{scene}}$  are not directly used, however, they may be used to construct a quality flag in the future.

$$\text{SCD} = \text{AMF}_c(P_{\text{scene}}, R_{\text{scene}}) \cdot \text{VCD}(P_{\text{scene}}) \quad (3)$$

$$I_{\text{TOA}} = I_{0b} + \frac{R_{\text{scene}} \cdot T_r}{1 - R_{\text{scene}} \cdot S_b} \quad (4)$$

The code for deriving cloud information from an observed spectrum and O<sub>2</sub>-O<sub>2</sub> SCD is adapted from the OMI cloud code (Vasilkov et al., 2018). The TEMPO adaptations include radiance and irradiance spectra, LUTs, GLER, meteorological inputs, and cloud output. New capabilities are developed to apply solar and radiance wavelength shift, O<sub>2</sub>-O<sub>2</sub> spectroscopic temperature correction, and ECF-OCP iteration.

### 3.2.2. Slant Column Density Retrieval

#### 3.2.2.1. Theoretical Basis for Spectral Fitting

The O<sub>2</sub>-O<sub>2</sub> SCD is retrieved by exploiting its spectral feature near 477 nm (Figure 2). The SCD retrieval uses the general-purpose SAO direct spectral fitting code that is shared among all molecules retrieved (González Abad et al., 2015). The code is applicable to trace gases with low optical depths which O<sub>2</sub>-O<sub>2</sub> satisfies. Slant columns are derived using non-linear least-squares minimization to directly fit a modeled radiance spectrum  $\mathbf{F}(\mathbf{x}, \mathbf{b})$  to an observed radiance spectrum  $\mathbf{y}$  through Levenberg-Marquart minimization of a cost function  $\chi^2$  (Equation 5),

$$\chi^2 = [\mathbf{y} - \mathbf{F}(\mathbf{x}, \mathbf{b})]^T \mathbf{S}_e^{-1} [\mathbf{y} - \mathbf{F}(\mathbf{x}, \mathbf{b})] \quad (5)$$

where  $\mathbf{S}_e$  is the covariance matrix of measurement errors, superscript  $T$  denotes transpose. In practice, errors on individual detector pixels in the detector array of the hyperspectral sounders are assumed to be uncorrelated, and thus  $\mathbf{S}_e$  is a diagonal matrix. The modeled spectrum is a function of input model parameters  $\mathbf{b}$  and the retrieved state vector  $\mathbf{x}$ . The modeled spectrum at each wavelength  $\lambda$  is represented by Equation 6,

$$F(\lambda) = [x_\alpha I_0(\lambda) + b_u(\lambda)x_u + b_r(\lambda)x_r + b_v(\lambda)x_v] \cdot e^{-\sum_i b_i(\lambda)x_i} \cdot \left( \sum_{j=0}^J (\lambda - \bar{\lambda})^j x_j^{SC} \right) + \left( \sum_{k=0}^K (\lambda - \bar{\lambda})^k x_k^{BL} \right) \quad (6)$$

where  $I_0$  is the solar irradiance observed by TEMPO scaled by a retrieved intensity parameter  $x_\alpha$  (which mainly represents the reflectance of the scene). The term  $b_u(\lambda)$  describes a correction for spectral under-sampling (Chance et al., 2005).  $b_r(\lambda)$  and  $b_v(\lambda)$  represent the effects of rotational and vibrational Raman scattering (i.e., the Ring and water Ring effect). The retrieved slant columns for the trace gas of interest and any spectrally interfering trace gases are represented by  $x_i$ . Their absorption cross sections convolved with the instrument slit function are included as  $b_i(\lambda)$ . In addition, the retrieval also determines the scaling (of order  $J$ ) and baseline (of order  $K$ ) polynomial coefficients  $x_j^{SC}$  and  $x_k^{BL}$  that represent low frequency wavelength-dependent effects from surface reflectivity, molecular scattering, aerosols and instrumental effects.  $\bar{\lambda}$  is the center of the retrieval window. The solar irradiance used in TEMPO retrieval is from the working diffuser solar observation that is nearest in time prior to the earthshine radiance observation.

#### 3.2.2.2. On-Orbit Spectral Calibration

Before the main spectral fitting, the TEMPO instrument line shape (i.e., slit function) is derived and the detector pixel-to-wavelength spectral calibration (solar wavelength shift) is refined by fitting the LIB irradiance spectrum to a simulated solar spectrum. The simulated solar spectrum is calculated using the Total and Spectral Solar

**Table 1**  
*Reference Spectra Used in TEMPO O<sub>2</sub>-O<sub>2</sub> SCD Fitting Algorithm*

Parameter	Details
NO <sub>2</sub>	Vandaele et al. (1998), 220 K
O <sub>3</sub>	Serdyuchenko et al. (2014), 223 K and 243K
O <sub>2</sub> -O <sub>2</sub>	Finkenzeller and Volkamer (2022), 223 K
H <sub>2</sub> O	HITRAN2020 (Gordon et al., 2022) 283 K, with <a href="https://hitran.org">hitran.org</a> updates as of February 2023
Liquid water LqH <sub>2</sub> O	Mason et al. (2016)
Under-sampling	Derived using Chance et al. (2005)
Ring effect	Calculated using Chance and Spurr (1997)
Water Ring effect	Chance and Spurr (1997)
Scaling polynomial	3rd order
Baseline polynomial	3rd order
Wavelength shift	Single value fitted on-line

Irradiance Sensor-1 (TSIS-1) high-resolution solar reference spectrum (Coddington et al., 2023) convolved with the instrument line shape.

The instrument line shape is parameterized using a super-Gaussian function (Equation 7) (Beirle et al., 2017; Sun et al., 2017) with three controlling parameters ( $w$ ,  $k$ , and  $\alpha_w$ ), where  $\Delta\lambda$  is the wavelength distance from the center of the instrument line shape function,  $\text{sgn}()$  is the sign function,  $w$  is the width parameter,  $k$  is the shape parameter,  $\alpha_w$  is the asymmetry parameter (currently assumed to be 0), and  $A_s$  is a normalization factor. We determine a single line shape function for the entire wavelength fitting window for each cross-track position of the CCD detector array. The line shape parameters are saved and applied to all the retrievals along the cross-track position of the granule.

$$s(\Delta\lambda) = A_s \cdot \exp \left[ - \left| \frac{\Delta\lambda}{w + \text{sgn}(\Delta\lambda)\alpha_w} \right|^k \right] \quad (7)$$

### 3.2.2.3. O<sub>2</sub>-O<sub>2</sub> Fitting Algorithm

The TEMPO O<sub>2</sub>-O<sub>2</sub> Slant Column Density (SCD) retrieval uses the fitting window of 439–488 nm. Table 1 lists the fitting algorithm details. The retrieval simultaneously fits slant column densities for NO<sub>2</sub>, O<sub>3</sub>, O<sub>2</sub>-O<sub>2</sub>, water vapor (H<sub>2</sub>O) and liquid water (LqH<sub>2</sub>O), as well as the Ring spectrum, vibrational Raman scattering (water Ring) spectrum, scaling and baseline closure polynomials, under-sampling correction, and a wavelength shift. As discussed before, the shape of the slit function is derived on-line using a super-Gaussian function. The fitted slit function is used to convolve high resolution trace gas reference spectra during fitting. Wavelength registration is refined using a constant shift from the wavelengths in the LIB file. The shift accounts for changes in pixel wavelength typically due to time-variable thermal changes in the instrument or inhomogeneous scenes (Voors et al., 2006).

Spectral pixels flagged as problematic (missing, bad, processing error, saturation) in LIB files are ignored during fitting. In addition, following the spike removal algorithm of Richter et al. (2011), after a spectral fitting, any detector pixels that show a greater than  $3\sigma$  deviation from the mean fitting residual are flagged, and the spectral fitting is repeated excluding those anomalous pixels.

Figure 3 shows the fitted O<sub>2</sub>-O<sub>2</sub> slant columns and their fitting uncertainties for the two scans in Figure 1. In general, the northern portion has larger SCDs because of larger air masses traversed. Areas with mid to high altitude clouds have smaller SCDs than their surroundings due to clouds that reflect light at higher altitudes than the surface. Areas with surface snow/ice or low altitude clouds have larger SCDs because of enhanced photon pathlengths due to multiple scattering between the bright surface and atmosphere (Vasilkov et al., 2010).

Over very bright clouds, spectra can show effects of partial or total saturation which leads to non-convergent fitting and missing SCDs (Figures 3c and 3d). The pixels adjacent to the failed retrievals tend to have



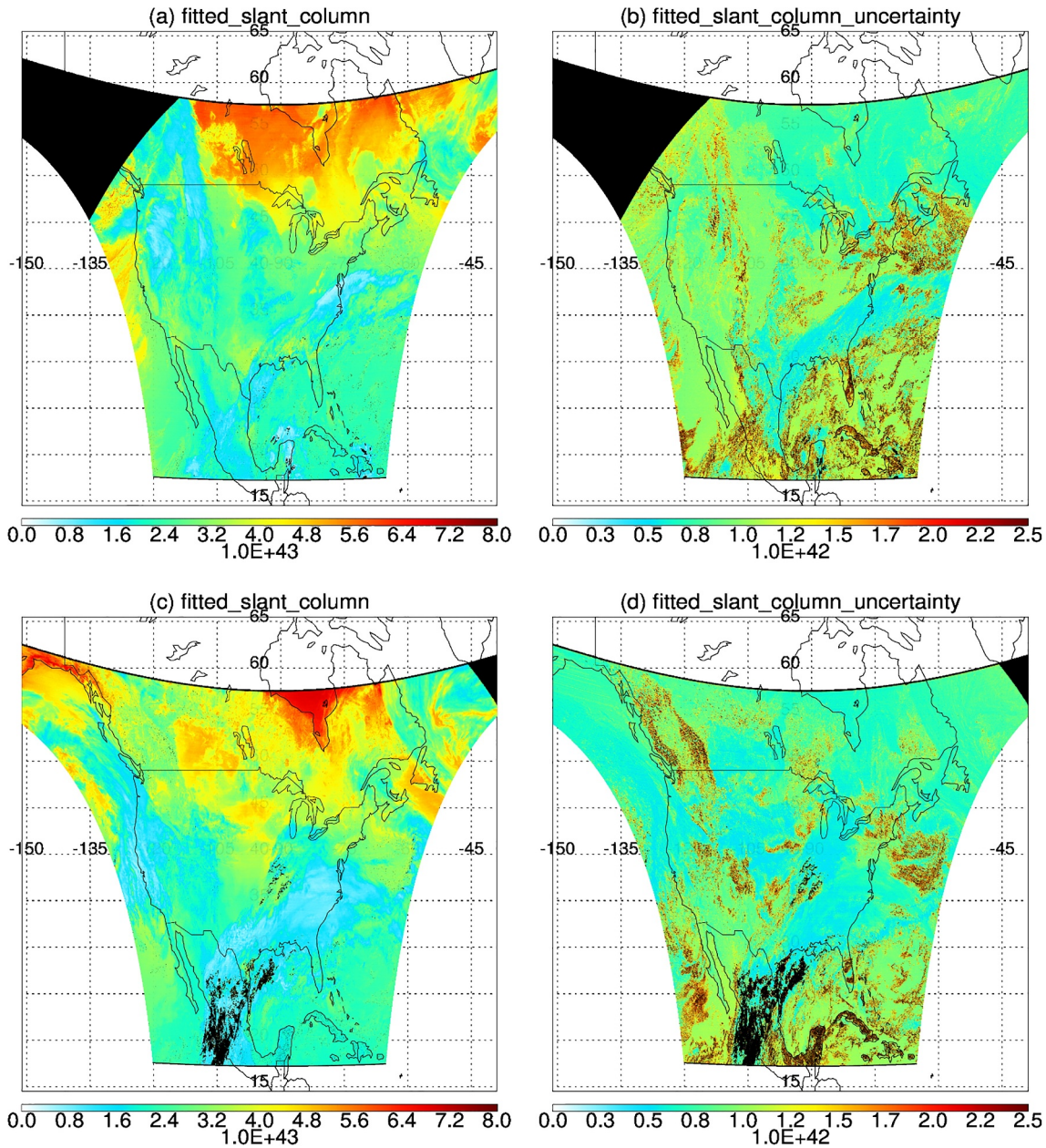


**Figure 3.** Fitted slant column SCD (molecule<sup>2</sup> cm<sup>-5</sup>, left) and the corresponding fitted slant column uncertainty (molecule<sup>2</sup> cm<sup>-5</sup>, right) for 11 November 2023 S006 (top) and 16 February 2024 S009 (bottom). Black areas in the northern part of the TEMPO field of regard have solar zenith angles SZA > 85°. Black pixels in (c, d) in the southern part indicate bad or suspicious retrievals.

unphysical (e.g., negative or extremely large) values and large fitting uncertainties. The fitting uncertainties are noticeably larger for non-homogeneous scenes associated with partially cloudy pixels (Noël et al., 2012) or land/water contrast and for large solar zenith angles (SZA > 85° are filtered out in Figure 3). For the example shown in Figure 3, the best relative fitting uncertainty (absolute fitting uncertainty/fitted SCD) of <1% is achieved over snow/ice surfaces where the absolute fitting uncertainties are small and the SCDs are large. Note, in Version 3 TEMPO CLDO4 product, fitted\_slant\_column\_uncertainty = 0 indicates bad retrievals instead of retrievals without uncertainty.

Figure 4 shows the statistics for the fitting Root Mean Squared (RMS) errors and fitting uncertainties for Figure 3.

The RMS is calculated as  $RMS = \sqrt{\left(\sum_{i=1}^m r_i^2\right)/m}$ , where  $m$  is the total number of spectral points used in the

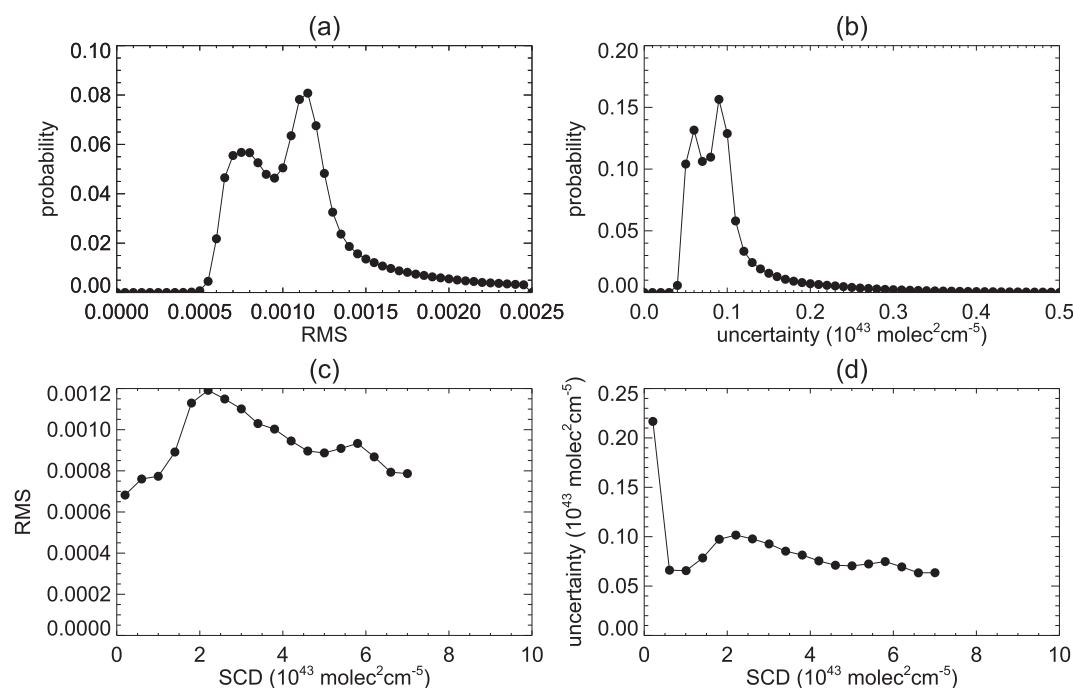


**Figure 4.** (top) Histograms of (a) fitting RMS and (b) absolute fitting uncertainty ( $\text{molecules}^2 \text{cm}^{-5}$ ). (c) Medium fitting RMS versus fitted SCD ( $\text{molecules}^2 \text{cm}^{-5}$ ). (d) Medium absolute fitting uncertainty ( $\text{molecules}^2 \text{cm}^{-5}$ ) versus fitted SCD ( $\text{molecules}^2 \text{cm}^{-5}$ ). Results in each panel are derived from Version 3 Level 2 TEMPO data for 11 November 2023 S006 and 16 February 2024 S009.

fitting and  $r_i$  is the fitting residual at each spectral point. The fitting uncertainty is calculated using the fitting RMS and covariance matrix's diagonal terms, with adjustment for degrees of freedom (number of spectral points—number of fitting parameters), as described in Chan Miller et al. (2014) and González Abad et al. (2016). The histograms at the top of Figure 4 show that the fitting RMS is mostly within the range from  $5.e - 4$  to  $1.5e - 3$  (Figure 4a) and the absolute fitting uncertainty is largely within  $3e + 41$  to  $2e + 42 \text{ molecule}^2 \text{cm}^{-5}$  (Figure 4b). As a function of SCD, the median fitting RMS varies around  $9.e - 4$  between  $7.e - 4$  and  $1.2e - 3$ , with a local maximum RMS occurring near  $\text{SCD} = 2.e + 43 \text{ molec}^2 \text{cm}^{-5}$  (Figure 4c). The medium absolute fitting uncertainty stays around  $7.e + 41 \text{ molecule}^2 \text{cm}^{-5}$  and varies between  $6.e + 41$  and  $1.e + 42 \text{ molecule}^2 \text{cm}^{-5}$  (except for very small SCDs) in a similar fashion (Figure 4d). The relative fitting uncertainty (i.e., fitting uncertainty/fitted SCD) is in general larger for smaller SCDs (due to smaller denominators).

### 3.2.2.4. $\text{O}_2\text{-O}_2$ Spectroscopic Temperature Correction

In SDPC V4.4, a single reference spectrum is used for the target molecule  $\text{O}_2\text{-O}_2$ . However, reference spectrum varies with temperature, which will influence the fitted SCD. Figure 5 shows the  $\text{O}_2\text{-O}_2$  reference spectrum (Finkenzeller & Volkamer, 2022) at 223 and 293 K. There is a main peak near 477 nm and a secondary peak near 446.5 nm. The lower temperature spectrum has sharper peaks, especially for the feature near 477 nm. The apparent change in spectral shape leads to differences in the retrieved SCD when  $\text{O}_2\text{-O}_2$  spectra at different temperatures are used. Thus, a post-fitting correction of SCD is employed to account for the effect of temperature on the  $\text{O}_2\text{-O}_2$  reference spectrum.

The approach described in the  $\text{O}_2\text{-O}_2$  SCD retrieval (Table 1) uses the  $\text{O}_2\text{-O}_2$  reference spectrum at 223 K. During the optimization for SCD fitting algorithm, we found that it usually leads to slightly smaller  $\text{O}_2\text{-O}_2$  fitting uncertainty than those at other temperatures. Due to the temperature dependence of the reference spectrum (Figure 5) (Finkenzeller & Volkamer, 2022), the retrieved  $\text{O}_2\text{-O}_2$  SCD can vary by a few percent, but results with different temperatures are highly correlated with coefficient of determination  $R^2 > 0.999$  (Table 2). Thus, a temperature correction of the retrieved SCD is performed iteratively according to Table 2.

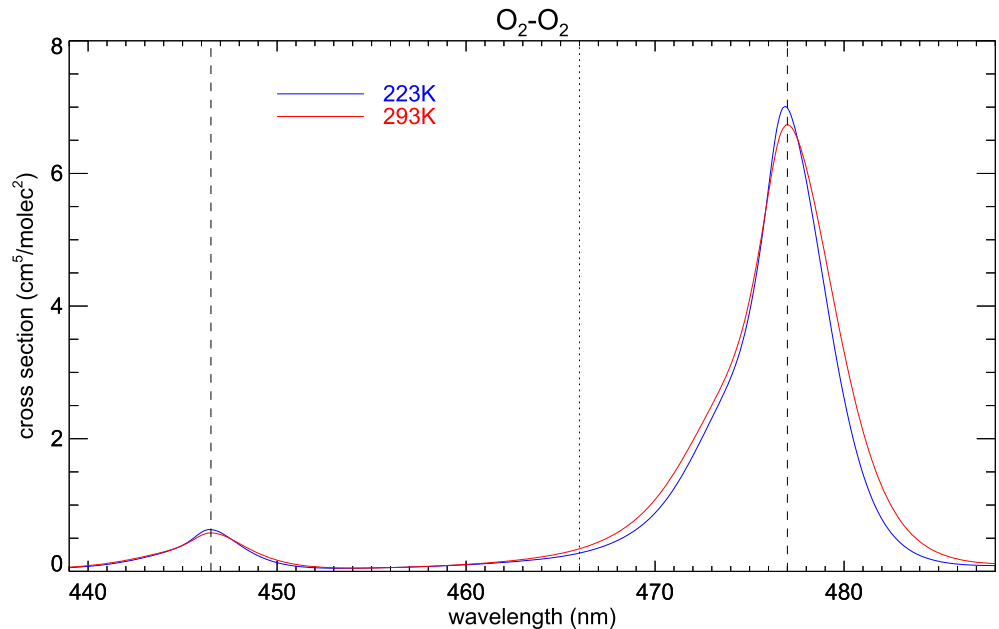


**Figure 5.** O<sub>2</sub>-O<sub>2</sub> cross section normalized by 10<sup>-46</sup> (cm<sup>5</sup>/molecule<sup>2</sup>) as a function of wavelength (nm) for (blue) 223 K and (red) 293 K. Dashed lines indicate peaks in the O<sub>2</sub>-O<sub>2</sub> spectra. Dotted line indicates 466 nm used for ECF retrieval.

For the SDPC v4.4 pipeline, the regression lines were derived from the SCDs retrieved using different reference temperatures for 29 September 2023 S007, and the correction is up to ~10% between 223 and 293 K for the specific fitting configuration listed in Table 1. Experiments for 11 November 2023 and 09 May 2024 show that the regression coefficients derived are similar (Table 2). The median SCDs adjusted using these alternative coefficients are well within 0.5% of those from the V4.4 SDPC coefficients.

Iteration starts with the O<sub>2</sub>-O<sub>2</sub> SCD retrieved from spectral fitting (Table 1), and the initial OCP is calculated from it. Then, the GEOS-CF T-P profile is used to calculate an effective temperature  $T_{\text{eff}}$  above the OCP. In V4.4 SDPC,  $T_{\text{eff}}$  adopts the temperature at an effective pressure of  $P_{\text{eff}} = 0.79 * \text{OCP}$ .  $T_{\text{eff}}$  is used to derive a corrected SCD which is in turn used to calculate a new OCP. The iteration continues until the change in  $T_{\text{eff}}$  is within 0.5 K or the maximum number of iterations (20) is reached. The factor 0.79 used for  $P_{\text{eff}}$  is chosen to be larger than 0.50 to account for O<sub>2</sub>-O<sub>2</sub>'s quadratic dependence on pressure. The actual effective temperature conceivably depends on the vertical sensitivity of the averaging kernel for O<sub>2</sub>-O<sub>2</sub>, which in turn depends on factors, such as reflectance, geometry, and aerosols. Furthermore, there are errors associated with the GEOS-CF T-P profiles. Thus, the optimal factor to use is yet to be determined. Future SDPC pipeline may include temperature for O<sub>2</sub>-O<sub>2</sub> as a parameter during spectral fitting, in which case, the temperature is used to calculate the reference spectrum which is in-turn used to convolve with the slit function. This approach will eliminate the need for a post-fitting SCD correction though the fitting will run slower.

**Table 2**  
O<sub>2</sub>-O<sub>2</sub> SCD Temperature Correction Relationships Derived From Different Scans

Date scan	T (K)	Regression line	R <sup>2</sup>
29 Sep 2023 S007	223	Y = X	1.0000
	263	Y = 1.049 * X + 0.010	0.9998
	293	Y = 1.103 * X + 0.017	0.9996
11 November 2023 S007	263	Y = 1.051 * X + 0.001	0.9999
	293	Y = 1.107 * X + 0.001	0.9999
09 May 2024 S007	263	Y = 1.053 * X + 0.000	0.9999
	293	Y = 1.109 * X + 0.001	0.9999

*Note.* The relationship used in V4.4 SDPC is shaded in blue. X and Y are the initial and corrected O<sub>2</sub>-O<sub>2</sub> SCDs in unit of 10<sup>43</sup> molecules<sup>2</sup>/cm<sup>5</sup>. Initial X is for 223 K.

### 3.3. Algorithm Implementation

The OMI cloud algorithm sequentially derives (1) cloud fraction (including ECF and CRF at 466 nm) and (2) cloud optical centroid pressure OCP, as the OCP calculation requires CRF as an input. During the initial ECF derivation, a cloud is assumed to be at 700 hPa which is usually different than the later retrieved OCP. However, it turns out that the  $I_c$  in Equation 1 is fairly insensitive to cloud pressure. This is illustrated by the right panel of Figure 6 where  $I_c$  is shown as a function of pressure and solar zenith angle (SZA) for a particular viewing zenith angle (VZA) and relative azimuth angle (RAA) pair. It can be seen that  $I_c$  values vary only slightly with pressure, especially for SZA > 60°. Nonetheless, there are some weak pressure dependences.

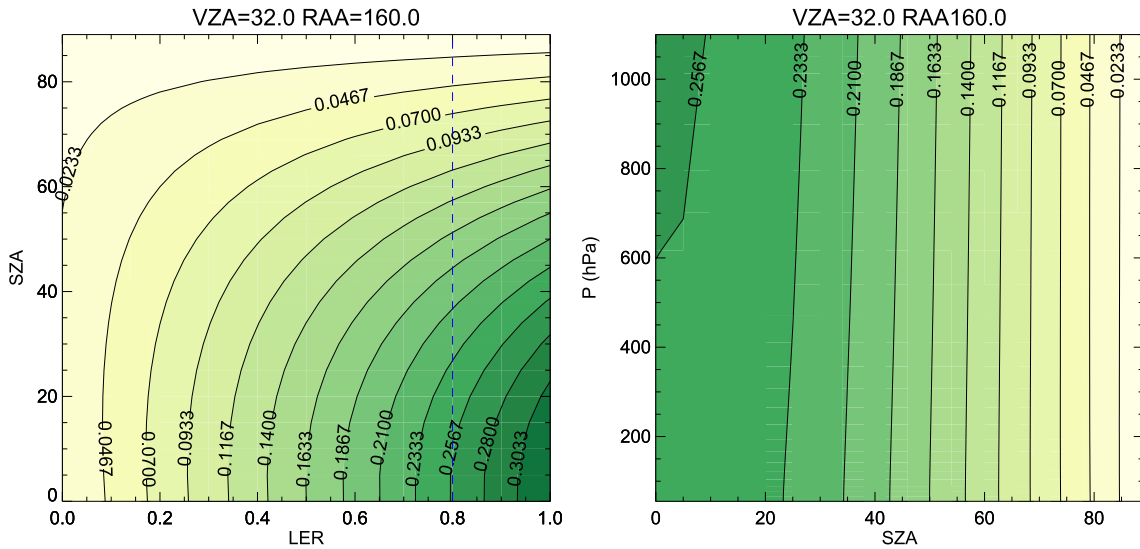


**Figure 6.** TOA 466 nm normalized radiance (i.e., radiance/irradiance) in the LUT calculated using the VLIDORT radiative transfer model. Left panel shows the result as a function of LER and SZA for VZA = 32°, RAA = 160°, and pressure of 1,013 hPa. Dashed line indicates LER = 0.8 which is assumed for clouds. Right panel shows the normalized radiance for clouds as a function of pressure and SZA for VZA = 32°, RAA = 160°, and LER = 0.8.

The TEMPO cloud algorithm thus iterates between ECF and OCP with a maximum of 5 iterations, where the OCP from Step (2) of each pass is used to derive the ECF in Step (1) of the next pass until ECF stabilizes within the neighborhood defined by the larger of 0.005 absolute value or 1% relative value and OCP stabilizes within the neighborhood of 1 hPa. The majority of TEMPO pixels only need a couple of iterations to converge, though some SZA and VZA combinations need more. A comparison between results obtained with and without iterations for 29 September 2023 S007 shows that the standard deviation of the differences for ECF is 0.017 and that for OCP is 13 hPa. As expected, the iterations preferentially affect the clouds at pressures away from 700 hPa.

ECF is determined by matching the observed and modeled TOA normalized radiance at 466 nm (Equation 1). For this purpose, the radiance and irradiance wavelength shifts obtained from the spectral fitting are applied to the LIB radiance and irradiance spectra, and the spectral values at 466 nm are extracted through linear interpolation using the two nearest wavelengths. As the radiance and irradiance are not simultaneously measured, a correction for the irradiance using the Sun-Earth distance squared ratio is also performed, though this correction is tiny as the irradiance is typically obtained within days of the radiance observation. The observed normalized radiance  $I_m$  is calculated as the ratio between the resultant 466 nm radiance and 466 nm irradiance.

$I_m$  is sensitive to the calibration of both the radiance and irradiance; errors related to calibration may bias  $I_m$  and subsequently the retrieved ECF and OCP. To demonstrate the influence of  $I_m$  error, Figure 7 shows the 25th, 50th, and 75th percentiles of the changes in ECF and OCP when  $I_m$  is reduced by 3% for 11 November 2023 S006. The SZAs for this scan vary from 35° to 89° and above, with a mean of 60°. For context, the normalized radiance derived from the Version 3 TEMPO LIB product may have a positive bias of up to 10% (Chong et al., 2025).

Figure 7 shows that the ECF values in the sensitivity test are reduced, and the influence is stronger for larger ECF. For ECF < 0.1, ECF values decrease by 0.01 for low and mid-altitude clouds and by 0.02 for high-altitude clouds. Accompanying changes in OCP are larger for smaller ECF, with OCP decreases for high-altitude clouds by >50 hPa and OCP increases for low-altitude clouds by >20 hPa when ECF is below 0.1. OCP changes for high ECFs are small (<5 hPa).

Calculation of the normalized TOA radiance employs the TEMPO OCP, GEOS-CF surface pressure, GLER and a pre-computed LUT at 466 nm. Under the assumption of Lambertian clouds with  $R_c = 0.8$  based on the OMI heritage (Vasilkov et al., 2018), clouds over darker surfaces ( $R_g < 0.8$ ) tend to make the scene brighter, and clouds over brighter surfaces ( $R_g > 0.8$ ) tend to make the scene darker. As an example, the left panel of Figure 6 shows the 466 nm TOA normalized radiance as a function of LER and SZA for VZA = 32°, RAA = 160°, and pressure

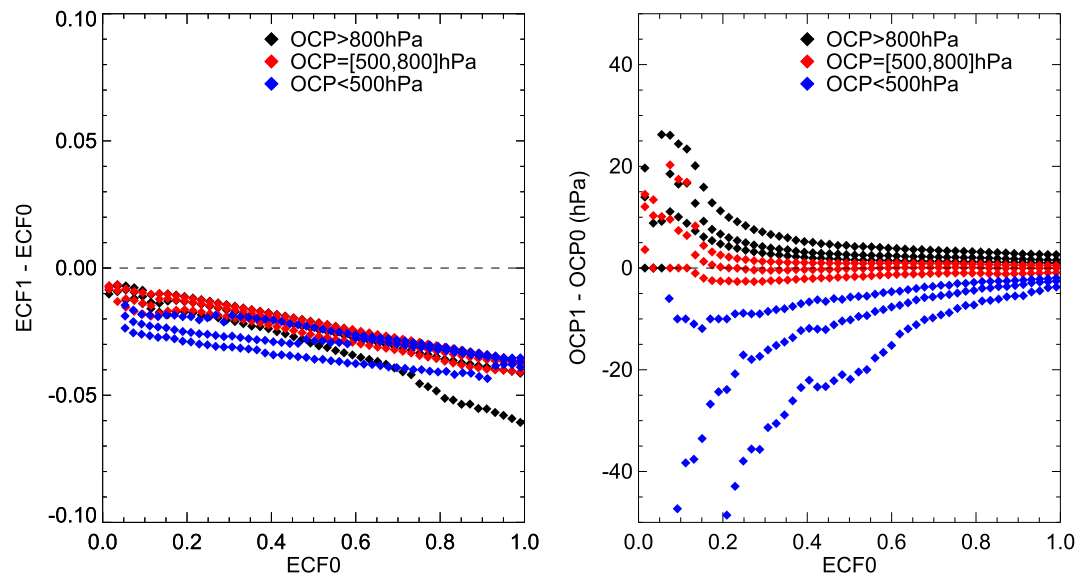


**Figure 7.** Influence of 466 nm  $I_m$  error on (left) ECF and (right) OCP. ECF0 and OCP0 are the reference values retrieved without any perturbation. ECF1 and OCP1 are the values retrieved using  $0.97^* I_m$ . Changes with respect to the reference values are plotted as a function of ECF0. Results are for 11 November 2023 S006 and are grouped according to (black) low-altitude  $p > 800$  hPa, (red) mid-altitude  $500 \text{ hPa} < p < 800$  hPa, and (blue) high-altitude  $p < 500$  hPa clouds. Each group contains three curves corresponding to the 25th, 50th, and 75th percentiles for the changes within each ECF0 bin.

$p = 1,013$  hPa. For non-snow/ice surface without glint, typical ground surface  $R_g$  ( $< 0.2$ ) is much smaller than the assumed cloud  $R_c$ , which leads to  $I_g < I_c$ . The ECF determined from  $f = (I_m - I_g)/(I_c - I_g)$  is within the normal range from 0 to 1 when  $I_g \leq I_m \leq I_c$ .

Note, the difference between  $I_c$  and  $I_g$  is smaller for larger SZA due to an increasingly larger contribution from the atmosphere. For  $\text{SZA} > 80^\circ$ , the calculated  $f$  is unreliable as  $I_g$  and  $I_c$  are hardly distinguishable. Similarly, for snow/ice surface or glint over water, the difference between  $R_g$  and  $R_c$  is small, which results in a reduced range between  $I_g$  and  $I_c$ . In this case, a small change in  $I_m$ ,  $I_g$ , or  $I_c$  will translate to a big change in  $f$ , leading to a large uncertainty in the result. When  $R_g = R_c$ ,  $I_g = I_c$ ,  $f$  is undefined, and clouds become indistinguishable from the surface based on the algorithm. When  $I_m$  is outside the range between  $I_g$  and  $I_c$ , the calculated  $f$  will be out of the nominal 0 to 1 range. In short, ECF is expected to have large errors for pixels with large surface reflectance and for pixels with large SZAs (or large geometric Air Mass Factors).

Stammes et al. (2008) showed that the reasonable choices of cloud LER are  $R_c = 0.8\text{--}0.9$ , with 0.8 being applicable on average, while 0.9 more favorable for bright clouds. Results from MODIS show that for inhomogeneous clouds, the optical thickness and therefore the reflectance of clouds appear larger for oblique views than for overhead views (Várnai & Marshak, 2007). Figure 8 shows the results of a sensitivity study for TEMPO can S007 on 29 September 2023 where the SZAs range from  $20^\circ$  to  $90^\circ$  with a mean of  $45^\circ$ . The results show that the ECF retrieved using  $R_c = 0.9$  is about 14% lower than that retrieved using  $R_c = 0.8$ . The OCP also changes accordingly, with the median OCP of high-altitude clouds becoming smaller by 10 hPa and that of low-altitude clouds becoming larger by 5 hPa. However, the median OCP of mid-altitude clouds changes very little, suggesting that they are the most robust with respect to the assumed cloud  $R_c$  in the retrieval.

To account for the variations in cloud reflectance, as well as the biases in surface reflectance and other prior inputs used to calculate the TOA normalized radiance, the retrieved ECF is allowed to go somewhat beyond the nominal range of  $[0.0, 1.0]$ . For the Version 3 TEMPO data, ECF is set to 0 when ECF is within the  $[-1.0, 0.0)$  range, and set to 1 when it is within the  $(1.0, 2.0]$  range. Bit 09 of the processing quality flags (Table 4) indicates whether ECF has been clipped (1) or not (0). A value of ECF beyond  $-1$  and  $2$  is considered to be unsuccessful retrieval and fill value is assigned in the data product to indicate that the algorithm has trouble reconciling the measurement with theoretical expectation. This usually indicates large errors in a priori inputs (e.g., surface reflectance),

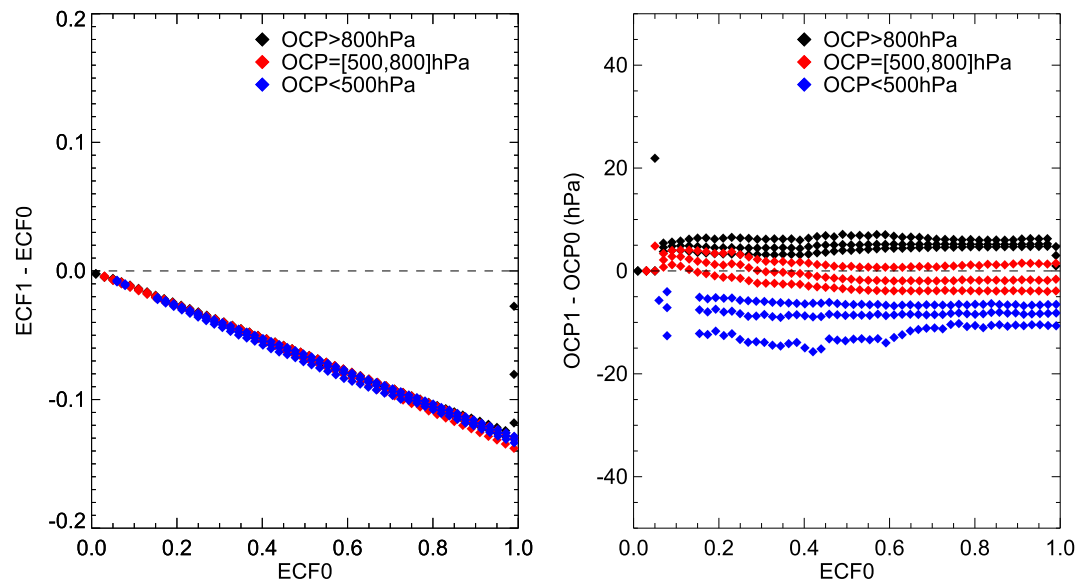


**Figure 8.** Influence of cloud  $R_c$  on (left) ECF and (right) OCP. ECF0 and OCP0 are the reference values retrieved using cloud  $R_c$  of 0.8. ECF1 and OCP1 are the values retrieved using cloud  $R_c$  of 0.9. Changes with respect to the reference values are plotted as a function of ECF0. Results are for 29 September 2023 S007 and are grouped according to (black) low-altitude  $p > 800$  hPa, (red) mid-altitude  $500 \text{ hPa} < p < 800$  hPa, and (blue) high-altitude  $p < 500$  hPa clouds. Each group contains three curves corresponding to the 25th, 50th, and 75th percentiles for the changes within each ECF0 bin.

problems with LIB data, inappropriate model assumptions (e.g., cloud reflectance), or large uncertainties. The currently arbitrary choice of the cutoffs ( $-1.0$  and  $2.0$ ) will be assessed in future studies.

OCP is determined by matching the retrieved and calculated  $\text{O}_2\text{-O}_2$  SCD (Equation 2). The retrieved SCD is obtained from the spectral fitting and spectroscopic temperature correction described before. The calculated SCD combines an overcast part and a clear-sky part weighted by the cloud radiance fraction CRF at  $466 \text{ nm}$ , where each SCD part is the product of the corresponding  $\text{O}_2\text{-O}_2$  VCD and AMF. We test the sensitivity of OCP to errors in the CRF by adding  $0.05$  to CRF for 29 September 2023 S007. This experiment is performed without ECF-OCP iteration, that is, ECF, CRF, and OCP are solved sequentially. Results in Figure 9 show that the overall standard deviation of the changes in OCP is about  $15 \text{ hPa}$ , with the OCP for low-altitude clouds being about  $15 \text{ hPa}$  smaller and the OCP for high altitude clouds about  $20 \text{ hPa}$  larger for  $0.2 < \text{ECF} < 0.8$ . The influence is stronger for  $\text{ECF} < 0.2$  where the medium change can exceed  $30 \text{ hPa}$  as ECF approaches 0. Among the three cloud groups, the change in OCP is the smallest for mid-altitude clouds.

Calculation of the  $\text{O}_2\text{-O}_2$  VCD employs the GEOS-CF temperature-pressure ( $T$ - $P$ ) profile, humidity-pressure ( $Q$ - $P$ ) profile, and surface pressure  $P_s$ . The VCD above the surface  $\text{VCD}(P_s)$  is calculated using Equation 8, where  $i = 0$  denotes the TOA,  $m(P_s)$  denotes the level corresponding to  $P_s$ ,  $Q$  is specific humidity in  $\text{kg/kg}$  or  $\text{g/g}$ ,  $T$  is temperature in  $\text{K}$ ,  $\Delta p_i$  denotes the pressure thickness ( $\text{hPa}$ ) of layer  $i$ ,  $C_f = 6.733e + 39 \text{ K hPa}^{-2} \text{ molecules}^2 \text{ cm}^{-5}$  is a conversion factor, and  $\text{O}_2\text{-O}_2$  VCD is in  $\text{molecule}^2 \text{ cm}^{-5}$ . The VCD above cloud  $\text{VCD}(P_c)$  is calculated using Equation 8 by replacing  $P_s$  with cloud optical centroid pressure  $P_c$ . Typical  $\text{O}_2\text{-O}_2$  VCD is on the order of  $10^{43} \text{ molecule}^2 \text{ cm}^{-5}$ . The AMF for clear (overcast) sky is interpolated from a pre-computed AMF LUT at  $477 \text{ nm}$  to the appropriate geometry, surface (cloud) reflectance and surface (cloud) pressure.

$$\text{VCD}(P_s) = C_f \cdot \frac{1}{2} \sum_{i=0}^{m(P_s)} \frac{(1-Q)^2 \Delta p_i^2}{T} \quad (8)$$

Veefkind et al. (2016) pointed out that, for very small cloud fractions, the information in the measurement is insufficient to accurately determine cloud pressure. In the Version 3 TEMPO L2 product, when  $\text{ECF} < 0.05$ , OCP is by default replaced by scene pressure. Bit 02 of the processing quality flag (Table 4) indicates whether the replacement has been done (1) or not (0). Veefkind et al. (2016) also recommends replacing cloud pressure with

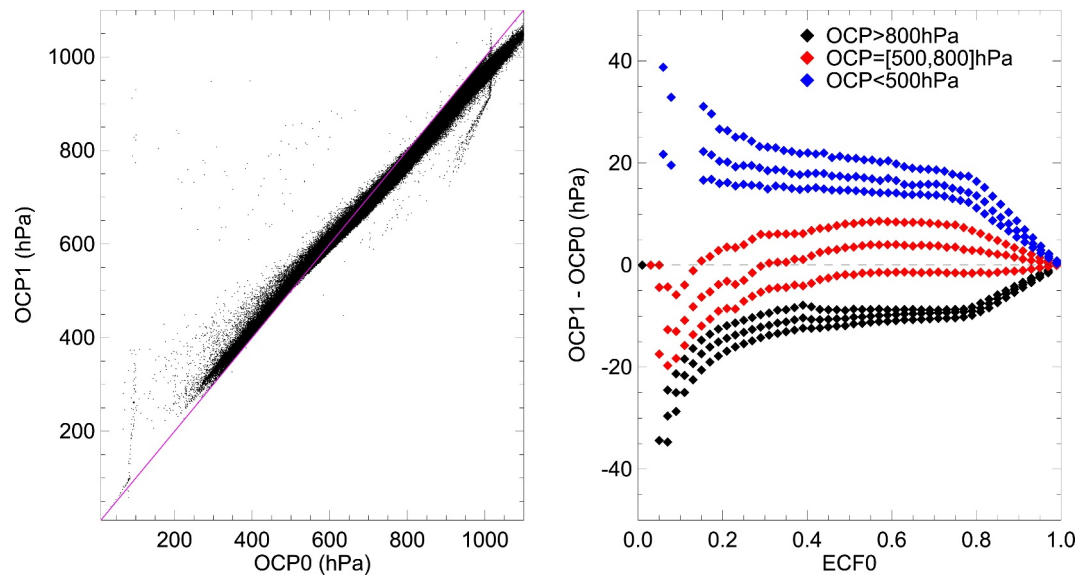


**Figure 9.** Sensitivity of OCP to CRF. OCP0 and ECF0 are from the reference retrieval without any perturbation. OCP1 is from the sensitivity run when CRF at 466 nm is increased by 0.05. Results are for 29 September 2023 S007. Left panel shows the scatter plot between OCP0 and OCP1. Right panel shows OCP1-OCP0 as a function of ECF0.

scene pressure over snow and ice surface because the retrieved OCP often becomes unstable. TEMPO Version 3 CLDO4 product currently retains OCP over snow and ice.

Figure 10 summarizes the TEMPO CLDO4 algorithm using a flow chart, illustrating the inputs, processing steps, and outputs.

### 3.4. Cloud Look Up Tables

Look Up Tables (LUTs) were calculated using the VLIDORT radiative transfer model Version 2.8.3 (Spurr & Christi, 2019). The calculation employed eight streams and 48 vertical levels for plane-parallel atmosphere with pseudo spherical correction and Lambertian surface reflectance. The LUTs are generated for dry air using the 1976 US standard atmosphere  $T$ - $P$  profile with 325 DU of ozone that is representative for the mid latitudes. The LUT construction employs the  $O_2$ - $O_2$  cross section from Thalman and Volkamer (2013), the  $O_3$  cross section from Serdyuchenko et al. (2014), and pre-flight TEMPO nominal slit function.

A LUT for the top of atmosphere normalized radiance (radiance/irradiance) at 466 nm was constructed to calculate the effective cloud fraction ECF and cloud radiance fraction CRF. The LUT depends on surface pressure  $P_s$ , Relative Azimuth Angle (RAA), Viewing Zenith Angle (VZA), Solar Zenith Angle (SZA), and LER. Clouds correspond to LER = 0.8. LUTs at 477 nm were created for AMFs under clear-sky and overcast conditions to calculate cloud optical centroid pressure OCP. The clear-sky AMF depends on  $P_s$ , RAA, VZA, SZA, and LER. The cloudy-sky AMF depends on  $P_s$ , cloud pressure ( $P_c$ ), RAA, VZA, and SZA. A LUT at 477 nm was also created for AMFs to calculate scene LER and scene pressure as a function of  $P_s$ ,  $P_c$ , RAA, VZA, SZA, and LER.

The nodes for the LUTs are listed in Table 3. The choices are based on Vasilkov et al. (2018)'s OMI study which seeks to keep interpolation error to <0.2%.

Veefkind et al. (2016) showed that, if the LUT constructed using a winter  $T$ - $P$  profile is used for summertime cloud retrieval, the retrieved OMI cloud pressure can be biased by 100 hPa or more for small cloud fractions ( $f < 0.1$ ), though the bias drops quickly to about 20 hPa when the cloud fraction increases to 0.3. To account for this bias, they implemented an SCD temperature correction which is different than the spectroscopic temperature correction described before. For Version 3 TEMPO CLDO4 data, all LUTs are based on a single  $T$ - $P$  profile which represents an average condition for all seasons, and the profile-related SCD temperature correction is not

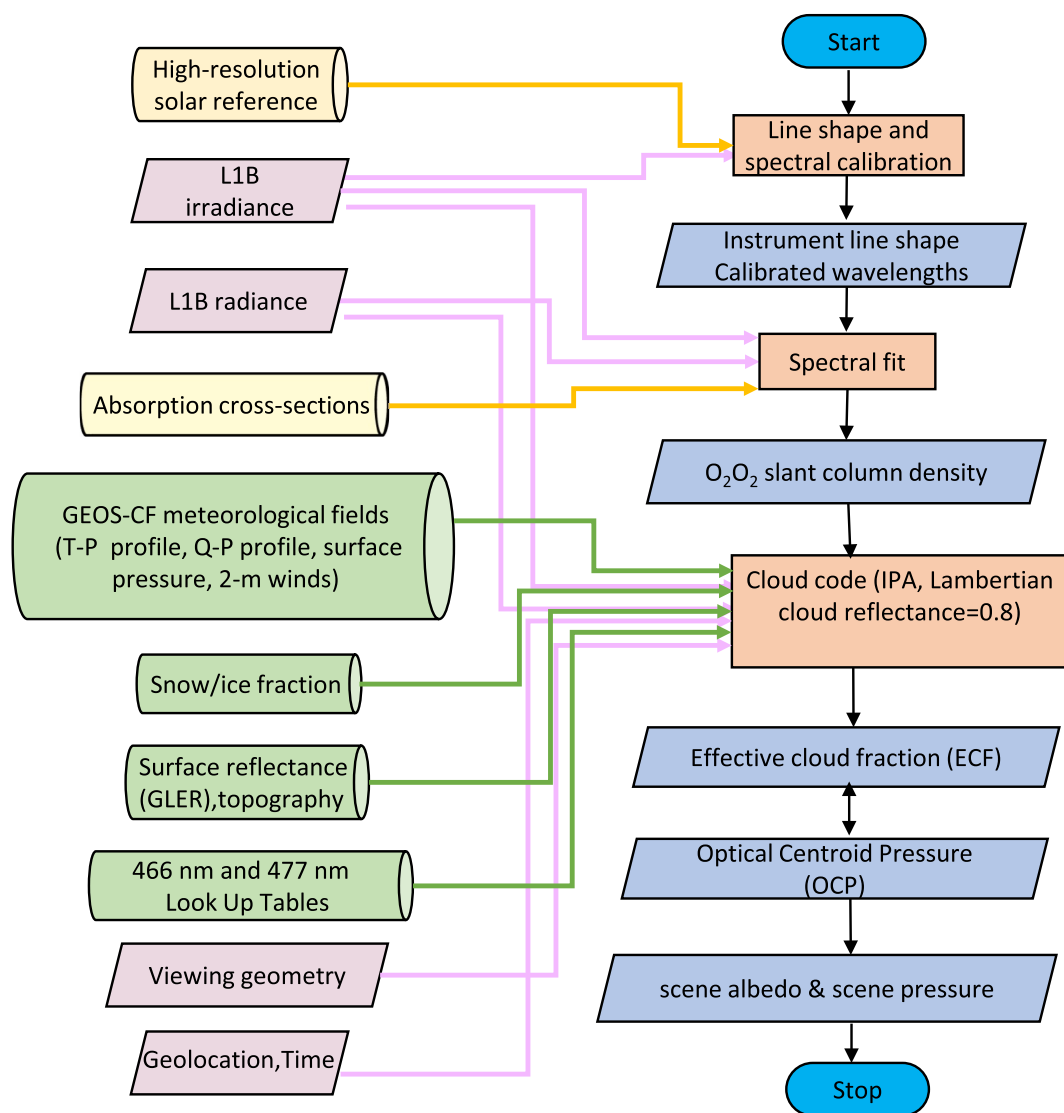


**Figure 10.** Flowchart for TEMPO CLDO4 algorithm. Purple boxes highlight TEMPO inputs. Green boxes highlight ancillary inputs and Look Up Tables. Yellow boxes highlight reference data. Orange boxes highlight code units. Blue boxes highlight outputs.

**Table 3**

Nodes for LUTs Used in TEMPO CLDO4 Retrieval

Parameter	Nodes
Solar Zenith Angle (SZA) (degree)	0, 5, 10, 15, 20, 25, 30, 34, 38, 42, 46, 50, 54, 57, 60, 63, 66, 69, 72, 75, 78, 80, 82, 84, 85, 86, 87, 88, 88.5, 89
Viewing Zenith Angle (VZA) (degree)	0, 4, 8, 12, 16, 20, 24, 28, 32, 36, 40, 44, 48, 52, 56, 60, 64, 68, 72, 75, 78, 81, 84, 87, 89
Relative Azimuth Angle (RAA) (degree)	0, 5, 10, 15, 20, 25, 30, 25, 40, 45, 50, 55, 60, 65, 70, 75, 80, 85, 90, 95, 100, 105, 110, 115, 120, 125, 130, 135, 140, 145, 150, 155, 160, 165, 170, 175, 180
LER	0.00, 0.01, 0.02, 0.04, 0.06, 0.08, 0.10, 0.12, 0.14, 0.16, 0.18, 0.20, 0.30, 0.40, 0.50, 0.60, 0.70, 0.80, 0.90, 1.00
Surface/cloud pressure (hPa)	1100, 1050, 1013, 899, 795, 701, 617, 541, 472, 411, 357, 308, 265, 227, 194, 166, 142, 121, 104, 89, 76, 65, 55



**Table 4**  
Meaning of Each bit of ProcessingQualityFlag for Version 3 TEMPO CLDO4 Data

bit	Meaning
bit 00	(Error) invalid latitude/longitude/SZA/VZA/RAA
bit 01	(Error) invalid 466 nm cloud radiance fraction
bit 02	(Warning) OCP is replaced by scene pressure because ECF < threshold (0.05)
bit 03	(Error) surface pressure or surface reflectance error
bit 04	(Warning) OCP is replaced by scene pressure as snow_ice_fraction > threshold (not activated in V4.4 SDPC)
bit 05	(Warning) SCD temperature correction problem during OCP calculation
bit 06	(Error) SCD < 0 or SCD quality issue
bit 07	(Warning) invalid 440 nm radiance, irradiance or CRF
bit 08	(Error) 466 nm radiance or irradiance error
bit 09	(Warning) ECF is out of the [0, 1] range and is clipped at the border (0 or 1)
bit 10	(Information) reserved for scene pressure code testing
bit 11	(Information) reserved for scene pressure code testing
bit 12	(Error) skipped ECF calculation due to any problem
bit 13	(Error) skipped OCP calculation due to any problem or invalid OCP
bit 14	(Warning) OCP is out of the LUT pressure range and is clipped at the nearest border of the LUT
bit 15	(Information) skipped scene pressure calculation due to any problem

applied. Note that the LUTs for TEMPO NO<sub>2</sub> and HCHO AMF calculations also employ the same US standard air T-P profile.

Figure 11 shows the influence of the changes in SCD on the retrieved OCP using a sensitivity run where the SCD is increased by 2% for 29 September 2023 S007. Results show that the OCP median increases in the sensitivity run by ~10 hPa for ECF > 0.2 and by up to 40 hPa for ECF < 0.2.

### 3.5. Ancillary Data

TEMPO CLDO4 requires a priori meteorological variables and surface reflectances. These inputs are based on the same data sets that are described in the TEMPO NO<sub>2</sub> and HCHO ATBDs (Gonzalez Abad et al., 2025; Nowlan et al., 2025). A brief overview is provided here.

Meteorological inputs for CLDO4 include surface pressure  $P_s$ , vertical humidity profile  $Q(p)$ , vertical temperature profile  $T(p)$ , and 2-m surface winds (U and V). These variables come from the GOES-CF products (Knowland et al., 2022) that are available at the time of SDPC processing. Typically, forecasts within 24 hr of TEMPO observations are used. Occasionally, forecasts on longer time spans are used if shorter ones are unavailable. A backup hourly climatology for each month derived from GEOS-CF is used if other options fail. The L2 file attribute “apriori\_source” indicates whether forecast or climatology is used. The meteorological variables are provided as instantaneous hourly fields at 0.25° longitude × 0.25° latitude resolution and are spatially and temporally interpolated for each TEMPO pixel.

To account for topography related difference in surface pressure between a TEMPO pixel and GEOS-CF model grid, an adjustment is made to surface pressure using the hypsometric equation  $P_2 = P_1 \cdot \exp[(z_1 - z_2)/(R_d \cdot T_v/g)]$ , where  $R_d = 287.05 \text{ J K}^{-1} \text{ kg}^{-1}$  is the gas constant of dry air,  $T_v = T \cdot (1 + 0.608 \cdot Q)$  is the virtual temperature at the surface,  $P_1$  is the surface pressure at height  $z_1$  (meter) from GEOS-CF, and  $P_2$  is the surface pressure at height  $z_2$  (meter) for the TEMPO pixel.

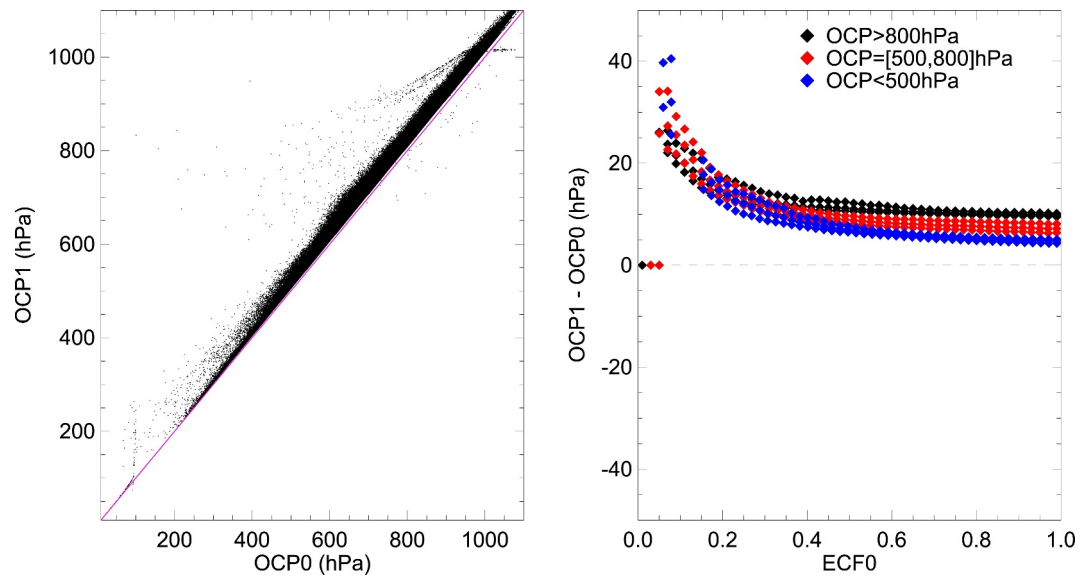


**Figure 11.** Influence of SCD on OCP for 29 September 2023 S007. OCP0 and ECF0 are from the reference run without any perturbations. OCP1 is from the sensitivity run where SCD is increased by 2%. Left panel shows the scatter plot. The 1:1 line is overplotted in red. Right panel shows the median of OCP1-OCP0 as a function for ECF0. Clouds at low-altitude, mid-altitude, and high-altitude are shown in black, red, and blue, respectively.

To estimate the sensitivity of cloud information to meteorological inputs, we compared the retrievals for 11 November 2023 S007 using an hourly climatology derived from GEOS-CF with that derived from Global Model Initiative (GMI, [earth.gsfc.nasa.gov/acd/models/gmi](http://earth.gsfc.nasa.gov/acd/models/gmi)) while keeping everything else the same. The results show little changes in ECF. For OCP, changes are small for ECF > 0.4, however, changes can be 20 hPa or more for ECF < 0.4.

Surface reflectance for TEMPO CLDO4 comes from the GLER module that is shared with NO<sub>2</sub> and HCHO algorithms in the SDPC. The GLER at the wavelength of interest and the time and location of each measurement is interpolated from a set of GLER LUTs. The LUTs for land surface contain the climatological GLERs at 0.05° × 0.05° resolution every 30 min for each month. The GLER LUTs are prepared off-line using the method described in Qin et al. (2019). As snow and ice can dramatically change surface albedo, the GLER over land is based on the MODIS climatology MCD43C1 (Schaaf & Wang, 2015a) and MCD43C2 (Schaaf & Wang, 2015b) for surfaces without and with snow/ice, respectively. The snow and ice fraction from the Interactive Multisensor Snow and Ice Mapping System (IMS, [usicecenter.gov/Products/ImsHome](http://usicecenter.gov/Products/ImsHome), US National Ice Center, 2008) is used to linearly combine the GLER of the snow-free and snow/ice part. The GLER over liquid water is based on the Cox-Munk slope function (Cox & Munk, 1954) driven by 2-m winds and water-leaving radiance with climatological chlorophyll distribution (Fasnacht et al., 2019). The spatial resolution of the GLER LUTs over the ocean is 1° × 1°.

ECF is affected by surface reflectance  $R_g$ . For a measured TOA normalized radiance  $I_m$ , an under-estimated  $R_g$  will lead to an over-estimated ECF as more clouds are needed to compensate for the difference, and vice versa. In other words, surface features will be aliased into the cloud fraction if the prescribed GLER is too low, conversely, cloud fraction will be biased low if surface is too bright. Figure 12 shows the influence of GLER on CLDO4 retrieval, where the GLER in the sensitivity run is increased by 0.01 for 29 September 2023 S007. The overall standard deviation of the changes in ECF is 0.004 and that in OCP is 29 hPa. However, the influence is non-uniform, and small ECF and high-altitude clouds are affected the most. For ECF < 0.1, ECF can decrease by 0.01 and OCP for high latitude clouds can decrease by >50 hPa. For ECF > 0.8, changes in ECF and OCP are small.

The current GLERs over land are based on MODIS climatology (Schaaf & Wang, 2015a, 2015b) derived from MODIS and Multi-angle Imaging SpectroRadiometer (MISR) observations. The accuracy of the climatology varies with geometry and larger solar zenith angles (or glint regions) generally have larger errors (Strahler et al., 1999). Thus, the GLERs used for Version 3 TEMPO product have non-uniform quality during the hours of

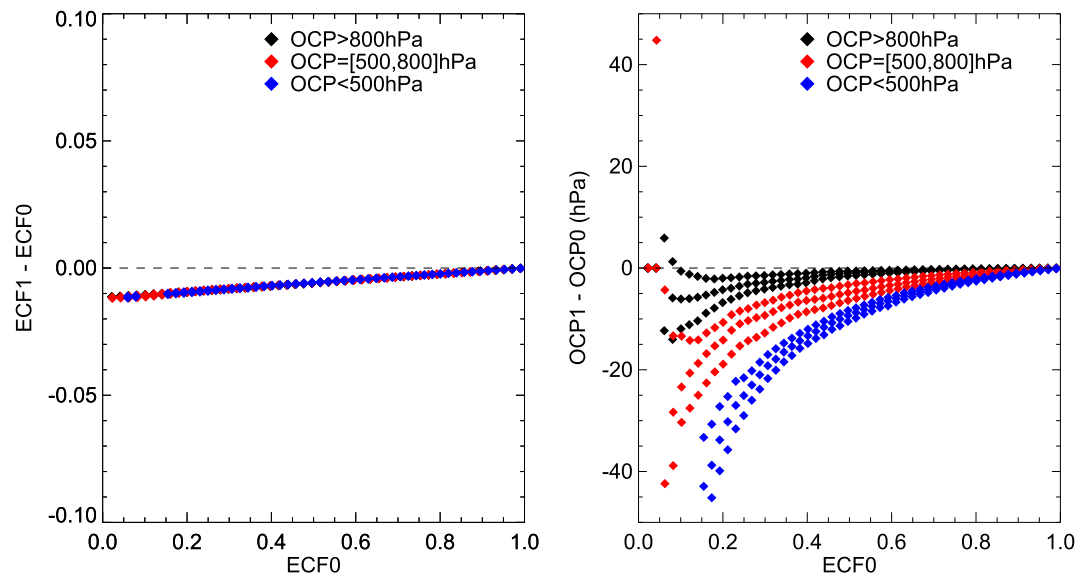


**Figure 12.** Sensitivity of (left) ECF and (right) OCP to GLER. ECF0 and OCP0 are from the reference retrieval. ECF1 and OCP1 are from the sensitivity retrieval where GLER is increased by 0.01. Median changes are plotted as a function of ECF0. High-altitude ( $p < 500$  hPa) clouds are in blue, mid-altitude ( $500 \text{ hPa} < p < 800$  hPa) clouds in red, and low-altitude ( $p > 800$  hPa) clouds in black.

TEMPO observations. In Version 3 TEMPO data, surface features (e.g., mountainous area) sometimes show up as clouds, suggesting GLER issues for at least some local times. For future data release, we plan to implement self-consistently derived GLER from TEMPO observations which cover the whole range of required geometries.

A rough estimate of the influence of surface reflectance is made through a sensitivity test where the OMI LER climatology (Kleipool et al., 2008) is used as  $R_g$  for 29 September 2023 S007. Results show that the standard deviation of the changes in ECF (sensitivity—reference) is 0.03 and that for OCP is 58 hPa. The changes preferentially affect small ECFs.

### 3.6. Quality Flags

The TEMPO CLDO4 algorithm in V4.4 SDPC pipeline does not calculate any formal quality flag for the retrieved cloud information, nor any uncertainty estimate for individual pixels. Any retrievals that failed for any reason are indicated by fill values in the product. Some caveats and cautions for usage of the data are provided in the user guide. Nonetheless, the following quality flags are provided in the Version 3 L2 files.

- a. SCD\_MainDataQualityFlag indicates the  $\text{O}_2\text{-O}_2$  SCD retrieval quality, with 0 meaning good, 1 meaning suspicious, and 2 meaning bad. A good retrieval has converged, is within the SCD range of 0 to  $1.0e + 44 \text{ molecule}^2 \text{ cm}^{-5}$ , and the fitted SCD is within 2 standard deviations ( $\sigma$ ) of the fitting uncertainty. A bad retrieval either has not converged, is out of allowed range, or is beyond  $3\sigma$ . A suspicious retrieval has converged, but the SCD is beyond  $2\sigma$ . In addition, retrievals with  $\text{SZA} > 89^\circ$  are all labeled suspicious. The SZA threshold above is intentionally relaxed to a high value of  $89^\circ$  to preserve as much potentially useful SCD data as possible. However, the fitting RMS increases rapidly for large SZAs ( $>70^\circ$ ). As an example, for 19 August 2023, the median fitting RMS for  $\text{SZA} < 60^\circ$  is about 0.0013. The median RMS increases to 0.0022 for  $\text{SZA} > 80^\circ$  which is about 70% larger. Furthermore, GLERs at large SZAs also have large errors. Consequently, cloud information derived at large SZAs tends to have large uncertainty, especially when ECF is low. The corresponding data should therefore be used with caution.

The influence of SZA on the sensitivity of OCP to ECF can be seen in Figure 13 where a comparison is made between the reference retrieval (OCP0) and a sensitivity run (OCP1) using S005 (morning scan), S009 (nominal scan), and S014 (evening scan) for 9 May 2024. The SZAs for morning and evening scans are generally larger than those for nominal scans. The sensitivity run calculates the OCPs when the ECFs are increased by 0.01 (without any ECF-OCP iteration). Figure 13a shows some large OCP changes. As indicated

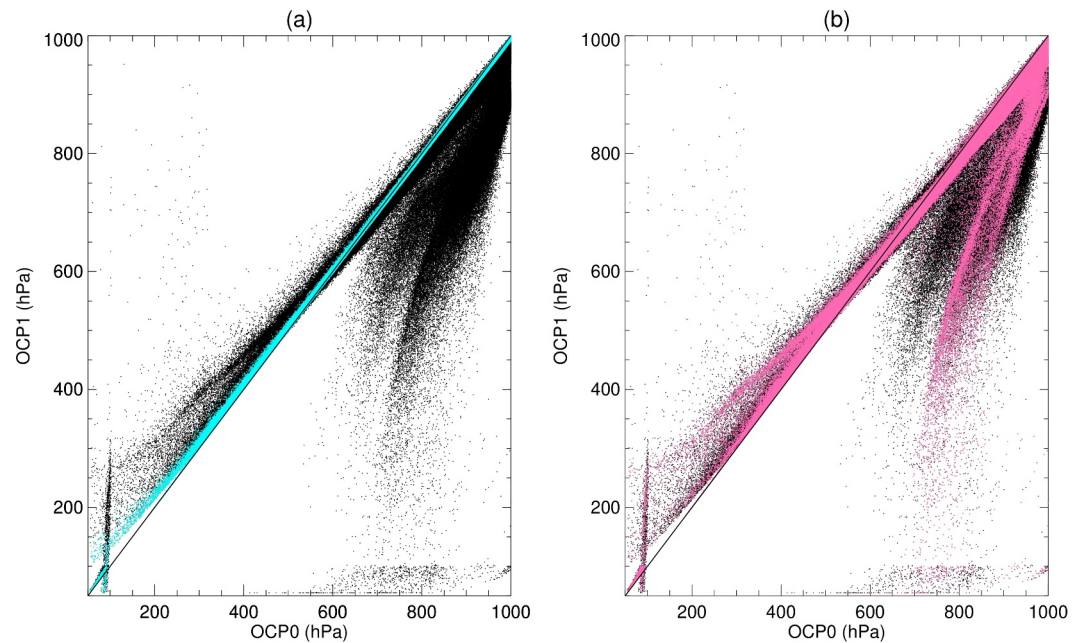


**Figure 13.** Sensitivity of OCP to ECF change derived from S005 (morning scan), S009 (nominal scan), and S014 (evening scan) for 9 May 2024. OCP0 values are from the reference retrieval. OCP1 values are from the sensitivity retrieval where ECF values are increased by 0.01. Black dots in both panels represent all data. Cyan dots in (a) represent the subset with the original ECF > 0.3. Pink dots in (b) represent the subset with SZA > 50°. The 1:1 line is plotted for reference.

by the data points far from the 1:1 line, low OCPs become larger and high OCPs become smaller. However, the subset for ECF > 0.3 (cyan) remains close to the 1:1 line (Figure 13a), thus, the large OCP changes are related to small ECFs. Figure 13b highlights the subset for SZA > 50° in pink and suggests that large OCP changes for small ECFs tend to be associated with large SZAs.

- b. `fit_convergence_flag` indicates whether the O<sub>2</sub>-O<sub>2</sub> SCD fitting has converged (1) or not (0).
- c. `ProcessingQualityFlag` is a 16-bit integer. Each bit (if set to 1) indicates a certain condition occurred during processing. The meaning of each bit for Version 3 TEMPO CLDO4 data is listed in Table 4. As all 16 bits are used, bitwise (instead of integer value) check is advised.

This flag is mainly constructed for code development, and it is not a formal quality flag for the product. As some bits may be of interest to users, the flag is included in the L2 product. This flag may change in future data release.

### 3.7. TEMPO CLDO4 Product Example

Figure 14 shows the retrieved ECF and OCP for the scans in Figure 1. A visual comparison shows that the cloud locations in the ECF maps are consistent with those in the color images. The ECFs in the upper left corner of Figure 14a are missing due to large geometric air mass factor as well as glint over the ocean. The missing patch of ECFs in Figure 14c is due to retrieval difficulty over snow and ice. Missing values in the OCP maps are primarily due to (a) ECF unavailable (b) SCD unavailable or unusable (c) no cloud present. There appears to be a general tendency of more clouds with lower OCP in the northern than in the southern part of the domain, which is consistent with the expectation that OCP is closer to the cloud top when geometric air mass factor is larger (Sneep et al., 2008).

Figure 15a shows the ECF histograms composed using all 13 daytime TEMPO scans on 16 February 2024. Different curves correspond to different geometric air mass factor  $AMF_{geo}$  bins. Results show a local maximum around 0.05, with the peak shifting slightly to the right with increasing  $AMF_{geo}$ .

Figure 15b shows the corresponding cloud radiance fraction CRF at 466 nm. As  $CRF = ECF * I_c / I_m$ , and generally  $I_c > I_m$ , the CRF peaks at a larger value around 0.2. The peaks for CRF also depend on  $AMF_{geo}$ , but the tendency is opposite to that of ECF, that is, CRF shifts to the left for larger  $AMF_{geo}$ .

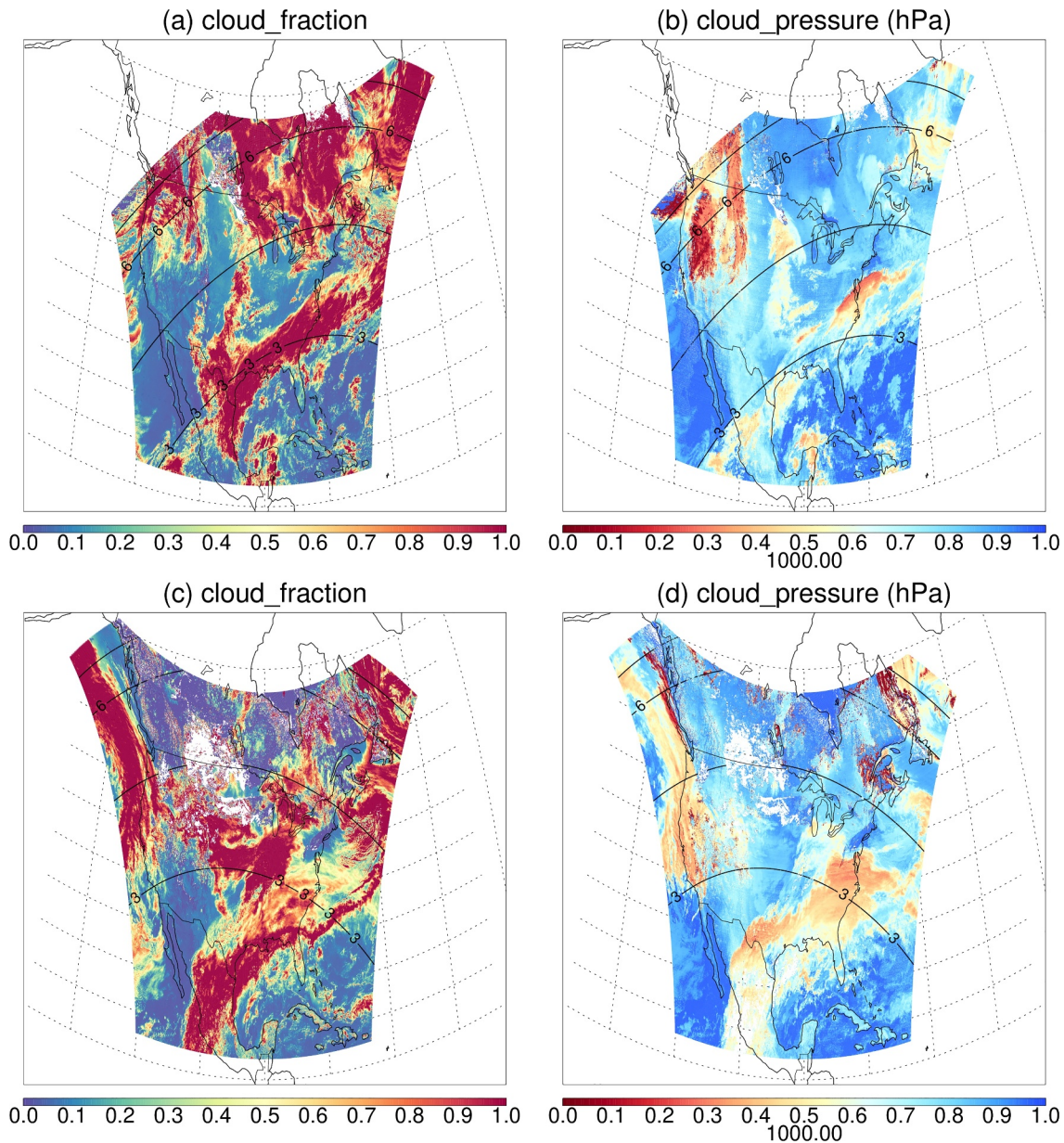


**Figure 14.** (a, c) ECF and (b, d) OCP (hPa) derived using TEMPO CLDO4 algorithm for (a, b) 11 November 2023 S006 and (c, d) 16 February 2024 S009. Black curves indicate geometric air mass factors for  $AMF_{geo} = 3, 4, 6, 8$ .

The local maxima in the TEMPO histograms are at odds with the general pattern derived from other sensors which shows monotonic decrease from 0 to 1 for partially cloudy scenes (Stammes et al., 2008; Vasilkov et al., 2018). Furthermore, trace gas validation for TEMPO suggests that the current TEMPO cloud fraction may have been overestimated (González Abad et al., 2025; Nowlan et al., 2025). Based on the sensitivity tests presented in previous sections, within the framework of this cloud algorithm, lower ECF can be achieved through (a) smaller L1B normalized radiance, (b) higher GLER (c) larger cloud  $R_c$ . As the OMI ECF derived using the  $R_c = 0.8$  assumption shows monotonically decreasing trend in the histogram from 0 to 1 (Stammes et al., 2008; Vasilkov et al., 2018), the former two factors are more relevant and are under investigation.

### 3.8. Assumptions

The following assumptions are made for Version 3 TEMPO CLDO4 retrieval:

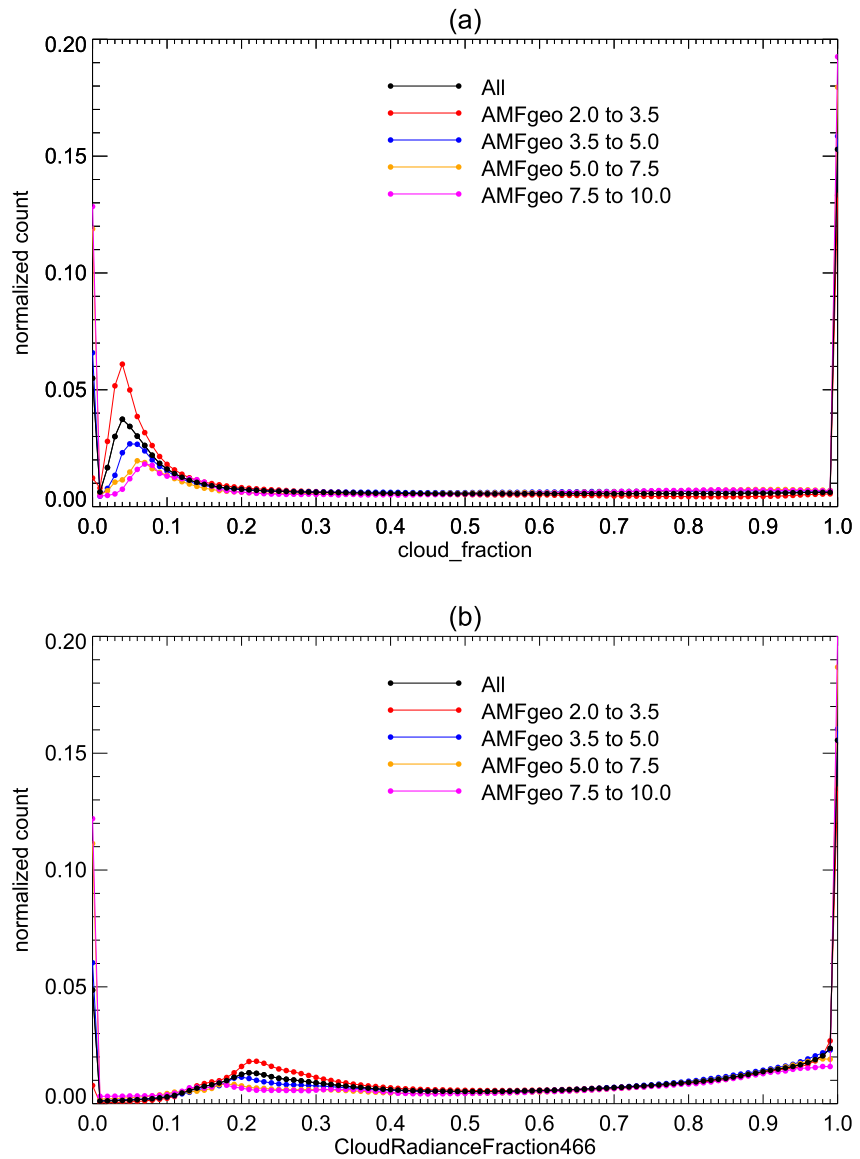


**Figure 15.** Histograms (normalized by total counts) of (a) ECF and (b) CRF at 466 nm derived from TEMPO scans S002 to S014 on 16 February 2024. Different colors correspond to different geometric air mass factor ( $AMF_{geo}$ ) bins as indicated by the legend.

1. Clouds are modeled as Lambertian surfaces with  $R_c = 0.8$ . Both ECF and OCP are controlled by this assumption.
2. Independent Pixel Approximation (IPA) is used where a pixel is assumed to be composed of a clear-sky part and a complementing overcast part.
3. The effect of aerosols is implicitly accounted for within the derived cloud information. In other words, aerosols affect the retrieved cloud information.
4. LUTs assume US standard air  $T$ - $P$  profile (1976) with 325 DU of ozone at mid latitude (M325) without any aerosols.
5. Radiative transfer calculations for CLDO4 LUT construction assume a plane-parallel atmosphere (with pseudo spherical correction) and Lambertian surface.
6. GLERs over land are based on MODIS climatology which employs kernels to approximate BRDFs. MODIS climatology is constrained with limited range of sun-satellite geometries, thus, its accuracy for TEMPO application remains to be tested.

7. GEOS-CF forecasts are used as a priori meteorological inputs.
8. When  $ECF < 0.05$ , OCP is replaced with scene pressure in Version 3 TEMPO data.

## 4. Performance Assessment Validation

### 4.1. Caveats

The TEMPO cloud product is primarily for supporting TEMPO trace gas retrievals. Intercomparisons with the cloud products from other instruments (e.g., TROPOMI, Visible Infrared Imaging Radiometer Suite (VIIRS), Advanced Baseline Imager (ABI), Earth Polychromatic Imaging Camera (EPIC)) can be made to check for general consistency. However, discrepancy is expected, and results should be interpreted with caution due to the following factors.

- (a) Different assumptions are made for different cloud products, such as IPA, treatment of a cloud as a Lambertian reflector with a fixed or variable albedo or as a scattering cloud volume.
- (b) Different choices are made for ancillary inputs (e.g.,  $T$ - $P$  profile, surface reflectance) that are used to derive cloud information. This so-called “structural error” (Lorente et al., 2017) can be a major source of error.
- (c) The geometric cloud fraction and cloud top are different from the effective cloud fraction and optical centroid pressure. From an instrument sensor's point of view, a thick cloud covering a fraction of a pixel can be confused with a thin overcast cloud or any combination of the two end members (Veeffkind et al., 2016). Multi-layered cloud configuration further complicates the interpretation (Joiner et al., 2010).
- (d) Cloud information strongly depends on the spatial resolution and retrieval method. The retrieved cloud fraction and cloud pressure are related to each other and work in pairs. For example, ECF and OCP are different for different cloud reflectance assumptions, but all solutions satisfy the same constraints of TOA normalized radiance and  $O_2-O_2$  SCD.

In short, simple direct inter-comparisons may not be appropriate for direct validation of the cloud products.

### 4.2. Simple Comparison

Notwithstanding the complications above, a rough consistency check is made between TEMPO and TROPOMI through a simple comparison in Figure 16. One TEMPO scan is compared with the TROPOMI swaths obtained over the TEMPO domain on the same day (28 March 2024).

While TROPOMI observes at a fixed overpass local time around 13:30, the TEMPO scan includes a range of local times from the east to the west. The first granule of the TEMPO scan is around 15:00 solar local time in the Atlantic and the last granule of the same scan is around 11:00 in the Pacific. The whole TEMPO scan covers 3 time zones and takes 1 hr to complete, which implies that the solar and viewing zenith angle coverages (and therefore the  $AMF_{geo}$  ranges) are different between TEMPO and TROPOMI.

As presented before, the retrieved cloud parameters have some  $AMF_{geo}$  dependence. Furthermore, different retrieval methods are used by TROPOMI and TEMPO. For TROPOMI, the `cloud_fraction_crb` represents the radiometric cloud fraction from the Optical Cloud Recognition Algorithm (OCRA)/Retrieval of Cloud Information using Neural Networks (ROCINN) Clouds as Reflecting Boundary (CRB) method (Latsch et al., 2022). For TEMPO, the `CloudRadianceFraction466` (CRF466) represents the cloud radiance fraction at 466 nm from the CLDO4 algorithm. Despite the differences mentioned above, the cloud patterns are consistent between TROPOMI and TEMPO. Detailed comparison through co-location is deferred to future work.

Figure 16 shows that the TROPOMI map contains seams and anomalous overlapping areas between consecutive swaths. While these may be due to temporal changes in clouds, they also coincide with changes in the  $AMF_{geo}$  between the left-hand side and right-hand side of each TROPOMI swath, therefore they could be partly related to differences in retrievals under different geometries as well. The TEMPO map in Figure 16 has noticeably larger values than TROPOMI for relatively clear conditions, which suggests that the TEMPO cloud fraction is biased high. The bias is also evident in the histograms. The TEMPO CRF466 (which is larger than ECF, as  $I_c/I_m > 1$  under most conditions) peaks around 0.2, while the TROPOMI histogram shows no apparent local peak between 0 and 1.

Based on the sensitivity tests presented previously, TEMPO's cloud fraction bias can potentially be corrected through improvements in the L1B data and surface GLER. For example, with a decrease of L1B radiance/

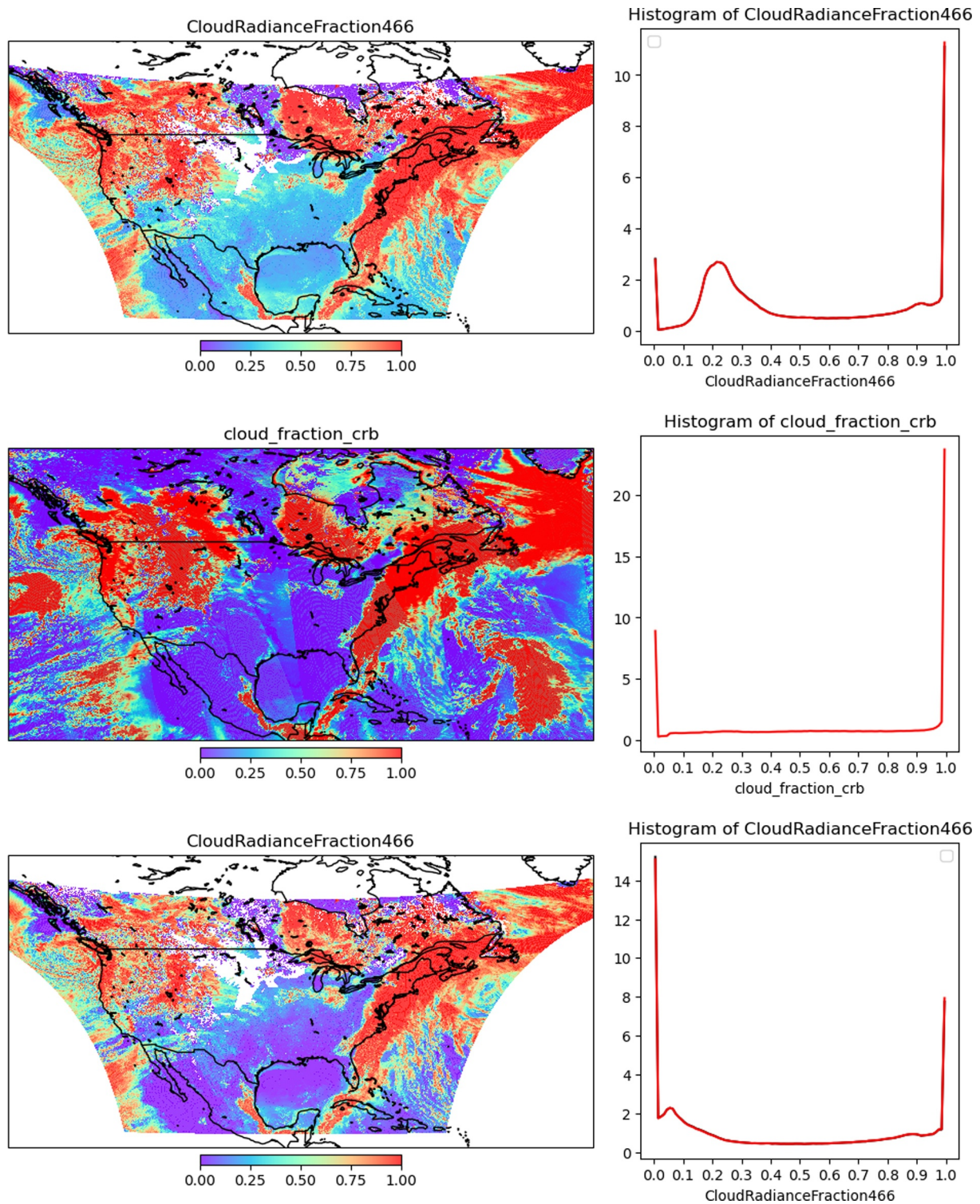


**Figure 16.** (left column) Maps and (right column) histograms of (top row) TEMPO CRF466 for 28 March 2024 S008 (middle row) TROPOMI cloud\_fraction\_crb within the extended TEMPO domain for 28 March 2024 (bottom row) TEMPO CRF466 for 28 March 2024 obtained in a sensitivity run where radiance/irradiance is reduced by 5% and GLER is increased by 0.02. Note, the TROPOMI histogram includes all the data within the domain shown.



irradiance ratio by 5% and an increase of GLER by 0.02, the TEMPO CRF466 histogram appears closer to that of TROPOMI. Note that the TROPOMI histogram includes all the data within the map, and the cloudy area over the oceans (where TEMPO did not cover) contributes to the high TROPOMI probability density at 1.

The TEMPO CLDO4 product has no planned formal validation effort. However, there is indirect validation through the TEMPO trace gas products. The trace gas validation report suggests that Version 3 TEMPO cloud fraction is biased high at least for some cases, which agrees with the result from the histogram analysis above.

Surface features sometimes appear to be aliased into TEMPO clouds (e.g., over mountainous region), which suggests that the GLER used is too low for those cases, consequently, the cloud algorithm needs to increase the ECF to compensate for the difference in TOA normalized radiance. On the one hand, as the same underlying GLER LUTs are implemented for both TEMPO CLDO4 and TEMPO trace gases, the GLER used for trace gas scattering weights (and therefore AMF) may also be biased low under these conditions, which tends to decrease the near-surface sensitivity. In this case, a larger (than actual) cloud fraction contributes through the cloudy part by increasing the sensitivity above the OCP so that the result of the overall trace gas AMF becomes closer to what is expected, had the surface GLER been prescribed higher. On the other hand, scattering weight is highly sensitive to clouds, this type of correction through clouds is prone to large errors. The cloud influence on AMF is further complicated by the shapes of trace gas profiles. The profile shape difference between trace gases and  $O_2-O_2$  is likely relevant in determining the sign and magnitude of errors associated with the AMF cloud part. It is thus best to have an accurate surface reflectance for both trace gas AMF and CLDO4 retrieval. The current GLERs over land are based on MODIS climatology which may not be applicable for the full range of TEMPO geometries. A surface GLER product derived from TEMPO observations has the potential to self-consistently improve both TEMPO CLDO4 and trace gas products in future data release.

## 5. Summary

The Version 3 TEMPO CLDO4 product is generated by SAO's Version 4.4 SDPC pipeline. The product is primarily for supporting TEMPO trace gas retrievals and contains cloud fraction (ECF and CRF) and cloud optical centroid pressure (OCP), among other variables. TEMPO cloud information is used to calculate AMFs and to perform data filtering for TEMPO trace gases (e.g.,  $NO_2$ , HCHO).

This paper describes the theoretical basis for spectral fitting and cloud information retrieval. The fitting employs SAO's general purpose code with an algorithm optimized for  $O_2-O_2$  SCD. The cloud information retrieval employs code adapted from the NASA OMI  $O_2-O_2$  cloud algorithm, with TEMPO specific development, such as input/output variables (spectra, meteorology, GLER), LUTs,  $O_2-O_2$  SCD temperature correction, and ECF-OCP iteration. The code implementation and data characteristics are discussed.

Sensitivity studies are performed to examine the influences of surface reflectance, cloud reflectance, L1B data, SCD, and meteorology on the retrieved ECF and OCP. In general, low ECFs, high-altitude clouds, and data for large SZAs are more sensitive to these error sources. The cloud information for high ECF is more robust.

It is noted that the ECF (and CRF) has a high bias for Version 3 TEMPO data, as the clear-sky pixels statistically peak near  $ECF = 0.05$  (Figure 15), whereas results from other sensors (e.g., OMI, TROPOMI) show a monotonically decreasing trend from 0. This offset is most likely linked to the absolute calibration of L1B data and surface GLER. In addition, as the CLDO4 LUTs are computed for a single representative condition, seasonal variations may be present. The materials presented in this paper provide the basis upon which future SDPC pipeline improvements will be made.

## Data Availability Statement

TEMPO Version 3 L2 and L3  $O_2-O_2$  cloud products (TEMPO\_CLDO4\_L2\_V03 and TEMPO\_CLDO4\_L3\_V03) are publicly available through NASA EarthData ASDC data center (<https://asdc.larc.nasa.gov/project/TEMPO>). Quick view of TEMPO products is available through NASA WorldView website (<https://worldview.gitc.uat.earthdatacloud.nasa.gov/>).

## Acknowledgments

TEMPO is NASA's first Earth Venture Instrument (EVI-1) project, led by Smithsonian Astrophysical Observatory (SAO) with project management at NASA Langley Research Center (LaRC) and instrument development at Ball Aerospace (now BAE systems). Support for TEMPO is from NASA TEMPO Grant NNL13AA09C and NASA SNWG TEMPO Near Real Time Grant 80MSFC24CA004. The TEMPO validation team supports trace gas validation effort. The Atmospheric Science Data Center (ASDC) at NASA LaRC supports dissemination of TEMPO products. This ATBD was originally prepared using NASA's Algorithm Publication Tool (APT) and later converted to paper format. The presentation flow thus roughly follows that defined by the APT. We thank Guyeon Kim, Ruijun Dang, and Luca Lelli for their thorough reviews.

## References

- Beirle, S., Lampel, J., Lerot, C., Sihler, H., & Wagner, T. (2017). Parameterizing the instrumental spectral response function and its changes by a super-Gaussian and its derivatives. *Atmospheric Measurement Techniques*, *10*(2), 581–598. <https://doi.org/10.5194/amt-10-581-2017>
- Boersma, K. F., Eskes, H. J., & Brinksma, E. J. (2004). Error analysis for tropospheric NO<sub>2</sub> retrieval from space. *Journal of Geophysical Research*, *109*(D4), D04311. <https://doi.org/10.1029/2003JD003962>
- Bovensmann, H., Burrows, J. P., Buchwitz, M., Frerick, J., Noël, S., Rozanov, V. V., et al. (1999). SCIAMACHY: Mission objectives and measurement modes. *Journal of the Atmospheric Sciences*, *56*(2), 127–150. [https://doi.org/10.1175/1520-0469\(1999\)056<0127:SMOAMM>2.0.CO;2](https://doi.org/10.1175/1520-0469(1999)056<0127:SMOAMM>2.0.CO;2)
- Burrows, J. P., Weber, M., Buchwitz, M., Rozanov, V., Ladstätter-Weissenmayer, A., Richter, A., et al. (1999). The global ozone monitoring experiment (GOME): Mission concept and first scientific results. *Journal of the Atmospheric Sciences*, *56*(2), 151–175. [https://doi.org/10.1175/1520-0469\(1999\)056<0151:TGOMEG>2.0.CO;2](https://doi.org/10.1175/1520-0469(1999)056<0151:TGOMEG>2.0.CO;2)
- Chance, K., Kurosu, T. P., & Sioris, C. E. (2005). Undersampling correction for array detector-based satellite spectrometers. *Applied Optics*, *44*(7), 1296–1304. <https://doi.org/10.1364/AO.44.001296>
- Chance, K. V., & Spurr, R. J. (1997). Ring effect studies: Rayleigh scattering, including molecular parameters for rotational Raman scattering, and the Fraunhofer spectrum. *Applied Optics*, *36*(21), 5224–5230. <https://doi.org/10.1364/AO.36.005224>
- Chang, F., Li, Z., & Ackerman, S. (2000). Examining the relationship between cloud and radiation quantities derived from satellite observations and model calculations. *Journal of Climate*, *13*(21), 3842–3859. [https://doi.org/10.1175/1520-0442\(2000\)013<3842:retrbca>2.0.co;2](https://doi.org/10.1175/1520-0442(2000)013<3842:retrbca>2.0.co;2)
- Chan Miller, C., González Abad, G., Wang, H., Liu, C., Kurosu, T., Jacob, D. J., & Chance, K. (2014). Clyoxal retrieval from the ozone monitoring instrument. *Atmospheric Measurement Techniques*, *7*(11), 3891–3907. <https://doi.org/10.5194/amt-7-3891-2014>
- Chong, H., Liu, X., Houck, J. C., Flittner, D. E., Carr, J. L., Hou, W., Davis, J. E., et al. (2025). Algorithm theoretical basis document for the TEMPO Level 0-1 processor.
- Coddington, O. M., Richard, E. C., Harber, D., Pilewskie, P., Woods, T. N., Snow, M., et al. (2023). Version 2 of the TSIS-1 hybrid solar reference spectrum and extension to the full spectrum. *Earth and Space Science*, *10*(3), e2022EA002637. <https://doi.org/10.1029/2022ea002637>
- Cox, C., & Munk, W. (1954). Measurement of the roughness of the sea surface from photographs of the Sun's glitter. *Journal of the Optical Society of America*, *44*(11), 838–850. <https://doi.org/10.1364/JOSA.44.000838>
- Fasnacht, Z., Vasilkov, A., Haffner, D., Qin, W., Joiner, J., Krotkov, N., et al. (2019). A geometry-dependent surface Lambertian-equivalent reflectivity product for UV-Vis retrievals—Part 2: Evaluation over open ocean. *Atmospheric Measurement Techniques*, *12*, 6749–6769. <https://doi.org/10.5194/amt-12-6749-2019>
- Finkenzeller, H., & Volkamer, R. (2022). O<sub>2</sub>-O<sub>2</sub> CIA in the gas phase: Cross-section of weak bands, and continuum absorption between 297–500 nm. *Journal of Quantitative Spectroscopy and Radiative Transfer*, *279*, 108063. <https://doi.org/10.1016/j.jqsrt.2021.108063>
- Flynn, L., Long, C., Wu, X., Evans, R., Beck, C. T., Petropavlovskikh, I., et al. (2014). Performance of the ozone mapping and profiler suite (OMPS) products. *Journal of Geophysical Research: Atmospheres*, *119*(10), 6181–6195. <https://doi.org/10.1002/2013JD020467>
- Gatebe, C., & King, M. (2016). Airborne spectral BRDF of various surface types (ocean, vegetation, snow, desert, wetlands, cloud decks, smoke layers) for remote sensing applications. *Remote Sensing of Environment*, *179*, 131–148. <https://doi.org/10.1016/j.rse.2016.03.029>
- González Abad, G., Vasilkov, A., Seftor, C., Liu, X., & Chance, K. (2016). Smithsonian astrophysical observatory ozone mapping profiler suite (SAO OMPS) formaldehyde retrieval. *Atmospheric Measurement Techniques*, *9*(7), 2797–2812. <https://doi.org/10.5194/amt-9-2797-2016>
- González Abad, G., Nowlan, C. R., Liu, X., Wang, H., & Chance, K. (2025). TEMPO formaldehyde retrieval algorithm theoretical basis document. NASA Algorithm Publication Tool. <https://doi.org/10.5067/OQ95W53OG514>
- González Abad, G., Liu, X., Chance, K., Wang, H., Kurosu, T. P., & Suleiman, R. (2015). Updated Smithsonian astrophysical observatory ozone monitoring instrument (SAO OMI) formaldehyde retrieval. *Atmospheric Measurement Techniques*, *8*(1), 19–32. <https://doi.org/10.5194/amt-8-19-2015>
- Gordon, I. E., Rothman, L. S., Hargreaves, R. J., Hashemi, R., Karlovets, E. V., Skinner, F. M., et al. (2022). The HITRAN2020 molecular spectroscopic database. *Journal of Quantitative Spectroscopy and Radiative Transfer*, *277*, 107949. <https://doi.org/10.1016/j.jqsrt.2021.107949>
- Joiner, J., Schoeberl, M. R., Vasilkov, A. P., Oreopoulos, L., Platnick, S., Livesey, N. J., & Levelt, P. F. (2009). Accurate satellite-derived estimates of the tropospheric ozone impact on the global radiation budget. *Atmospheric Chemistry and Physics*, *9*(13), 4447–4465. <https://doi.org/10.5194/acp-9-4447-2009>
- Joiner, J., Vasilkov, A., Bhartia, P. K., Wind, G., Platnick, S., & Menzel, W. P. (2010). Detection of multi-layered clouds using A-train sensors. *Atmospheric Measurement Techniques*, *3*(1), 233–247. <https://doi.org/10.5194/amt-3-233-2010>
- Joiner, J., Vasilkov, A. P., Gupta, P., Bhartia, P. K., Veefkind, P., Snee, M., et al. (2012). Fast simulators for satellite cloud optical centroid pressure retrievals; evaluation of OMI cloud retrievals. *Atmospheric Measurement Techniques*, *5*(3), 529–545. <https://doi.org/10.5194/amt-5-529-2012>
- Kleipool, Q. L., Dobber, M. R., de Haan, J., & Levelt, P. F. (2008). Earth surface reflectance climatology from 3 years of OMI data. *Journal of Geophysical Research*, *113*(D18), D18308. <https://doi.org/10.1029/2008JD010290>
- Knowland, K. E., Keller, C. A., Wales, P. A., Wargan, K., Coy, L., Johnson, M. S., et al. (2022). NASA GEOS composition forecast modeling system GEOS-CF v1.0: Stratospheric composition. *Journal of Advances in Modeling Earth Systems*, *14*(6), e2021MS002852. <https://doi.org/10.1029/2021MS002852>
- Kobayashi, T. (1993). Effects due to cloud geometry on biases in the albedo derived from radiance measurements. *Journal of Climate*, *6*(1), 120–128. [https://doi.org/10.1175/1520-0442\(1993\)006<0120:EDTCGO>2.0.CO;2](https://doi.org/10.1175/1520-0442(1993)006<0120:EDTCGO>2.0.CO;2)
- Latsch, M., Richter, A., Eskes, H., Snee, M., Wang, P., Veefkind, P., et al. (2022). Intercomparison of Sentinel-5P TROPOMI cloud products for tropospheric trace gas retrievals. *Atmospheric Measurement Techniques*, *15*(21), 6257–6283. <https://doi.org/10.5194/amt-15-6257-2022>
- Levelt, P. F., Van Den Oord, G. H., Dobber, M. R., Malkki, A., Visser, H., De Vries, J., et al. (2006). The ozone monitoring instrument. *IEEE Transactions on Geoscience and Remote Sensing*, *44*(5), 1093–1101. <https://doi.org/10.1109/TGRS.2006.872333>
- Lorente, A., Folkert Boersma, K., Yu, H., Dörner, S., Hilboll, A., Richter, A., et al. (2017). Structural uncertainty in air mass factor calculation for NO<sub>2</sub> and HCHO satellite retrievals. *Atmospheric Measurement Techniques*, *10*(3), 759–782. <https://doi.org/10.5194/amt-10-759-2017>
- Martin, R. V., Chance, K., Jacob, D. J., Kurosu, T. P., Spurr, R. J., Bucsel, E., et al. (2002). An improved retrieval of tropospheric nitrogen dioxide from GOME. *Journal of Geophysical Research*, *107*(D20), 4437. <https://doi.org/10.1029/2001JD001027>
- Mason, J. D., Cone, M. T., & Fry, E. S. (2016). Ultraviolet (250–550 nm) absorption spectrum of pure water. *Applied Optics*, *55*(25), 7163–7172. <https://doi.org/10.1364/AO.55.007163>
- Munro, R., Lang, R., Klaes, D., Poli, G., Retscher, C., Lindstrot, R., et al. (2016). The GOME-2 instrument on the Metop series of satellites: Instrument design, calibration, and level 1 data processing—an overview. *Atmospheric Measurement Techniques*, *9*(3), 1279–1301. <https://doi.org/10.5194/amt-9-1279-2016>

- Noël, S., Bramstedt, K., Bovensmann, H., Gerilowski, K., Burrows, J. P., Standfuss, C., et al. (2012). Quantification and mitigation of the impact of scene inhomogeneity on Sentinel-4 UVN UV-VIS retrievals. *Atmospheric Measurement Techniques*, 5(6), 1319–1331. <https://doi.org/10.5194/amt-5-1319-2012>
- Nowlan, C. R., González Abad, G., Liu, X., Wang, H., & Chance, K. (2025). TEMPO nitrogen dioxide retrieval algorithm theoretical basis document. NASA Algorithm Publication Tool. <https://doi.org/10.5067/8YMVQJZZP6S2>
- Palmer, P. I., Jacob, D. J., Chance, K., Martin, R. V., Spurr, R. J., Kurosu, T. P., et al. (2001). Air mass factor formulation for spectroscopic measurements from satellites: Application to formaldehyde retrievals from the Global Ozone Monitoring Experiment. *Journal of Geophysical Research*, 106(D13), 14539–14550. <https://doi.org/10.1029/2000JD900772>
- Qin, W., Fasnacht, Z., Haffner, D., Vasilkov, A., Joiner, J., Krotkov, N., et al. (2019). A geometry-dependent surface Lambertian-equivalent reflectivity product for UV-Vis retrievals—Part 1: Evaluation over land surfaces using measurements from OMI at 466 nm. *Atmospheric Measurement Techniques*, 12(7), 3997–4017. <https://doi.org/10.5194/amt-12-3997-2019>
- Richter, A., Begoin, M., Hilboll, A., & Burrows, J. P. (2011). An improved NO<sub>2</sub> retrieval for the GOME-2 satellite instrument. *Atmospheric Measurement Techniques*, 4(6), 1147–1159. <https://doi.org/10.5194/amt-4-1147-2011>
- Schaaf, C., & Wang, Z. (2015a). MCD43C1 MODIS/Terra+Aqua BRDF/Albedo Model Parameters Daily L3 Global 0.05Deg CMG V006. <https://doi.org/10.5067/MODIS/MCD43C1.006>
- Schaaf, C., & Wang, Z. (2015b). MCD43C2 MODIS/Terra+Aqua BRDF/Albedo Snow-free Model Parameters Daily L3 Global 0.05Deg CMG V006. <https://doi.org/10.5067/MODIS/MCD43C2.006>
- Serdyuchenko, A., Gorshelev, V., Weber, M., Chehade, W., & Burrows, J. P. (2014). High spectral resolution ozone absorption cross-sections—Part 2: Temperature dependence. *Atmospheric Measurement Techniques*, 7(2), 625–636. <https://doi.org/10.5194/amt-7-625-2014>
- Sneep, M., De Haan, J. F., Stammes, P., Wang, P., Vanbauce, C., Joiner, J., et al. (2008). Three-way comparison between OMI and PARASOL cloud pressure products. *Journal of Geophysical Research*, 113(D15), D15S23. <https://doi.org/10.1029/2007JD008694>
- Spurr, R., & Christi, M. (2019). The LIDORT and VLIDORT linearized scalar and vector discrete ordinate radiative transfer models: Updates in the last 10 years. In *Springer Series in light scattering: Volume 3: Radiative transfer and light scattering* (pp. 1–62).
- Stammes, P., Sneep, M., De Haan, J. F., Veeffkind, J. P., Wang, P., & Levelt, P. F. (2008). Effective cloud fractions from the ozone monitoring instrument: Theoretical framework and validation. *Journal of Geophysical Research*, 113(D16), D16S38. <https://doi.org/10.1029/2007JD008820>
- Strahler, A. H., Lucht, W., Schaaf, C. B., Tsang, T., Gao, F., Li, X., et al. (1999). MODIS BRDF/albedo product: Algorithm theoretical basis document V5.0.
- Sun, K., Liu, X., Huang, G., González Abad, G., Cai, Z., Chance, K., & Yang, K. (2017). Deriving the slit functions from OMI solar observations and its implications for ozone-profile retrieval. *Atmospheric Measurement Techniques*, 10, 3677–3695. <https://doi.org/10.5194/amt-10-3677-2017>
- Thalman, R., & Volkamer, R. (2013). Temperature dependent absorption cross-sections of O<sub>2</sub>-O<sub>2</sub> collision pairs between 340 and 630 nm and at atmospherically relevant pressure. *Physical Chemistry Chemical Physics*, 15(37), 15371–15381. <https://doi.org/10.1039/c3cp50968k>
- U.S. National Ice Center. (2008). *I.M.S. daily Northern Hemisphere snow and ice analysis at 1 km, 4 km and 24 km resolutions, Version 1*. National Snow Ice Data Center. <https://doi.org/10.7265/N52R3PMC>
- Vandaele, A. C., Hermans, C., Simon, P. C., Carleer, M., Colin, R., Fally, S., et al. (1998). Measurements of the NO<sub>2</sub> absorption cross-section from 42 000 cm<sup>-1</sup> to 10 000 cm<sup>-1</sup> (238–1000 nm) at 220 K and 294 K. *Journal of Quantitative Spectroscopy and Radiative Transfer*, 59(3–5), 171–184. [https://doi.org/10.1016/S0022-4073\(97\)00168-4](https://doi.org/10.1016/S0022-4073(97)00168-4)
- Várnai, T., & Marshak, A. (2007). View angle dependence of cloud optical thicknesses retrieved by Moderate Resolution Imaging Spectroradiometer (MODIS). *Journal of Geophysical Research*, 112(D6), D06203. <https://doi.org/10.1029/2005JD006912>
- Vasilkov, A., Joiner, J., Haffner, D. P., Bhartia, P. K., & Spurr, R. J. D. (2010). What do satellite backscatter ultraviolet and visible spectrometers see over snow and ice? A study using the A-train. *Atmospheric Measurement Techniques*, 3(3), 619–629. <https://doi.org/10.5194/amt-3-619-2010>
- Vasilkov, A., Joiner, J., Spurr, R., Bhartia, P. K., Levelt, P., & Stephens, G. (2008). Evaluation of the OMI cloud pressures derived from rotational Raman scattering by comparisons with other satellite data and radiative transfer simulations. *Journal of Geophysical Research*, 113, D15. <https://doi.org/10.1029/2007JD008689>
- Vasilkov, A., Joiner, J., Yang, K., & Bhartia, P. K. (2004). Improving total column ozone retrievals by using cloud pressures derived from Raman scattering in the UV. *Geophysical Research Letters*, 31, 20. <https://doi.org/10.1029/2004GL020603>
- Vasilkov, A., Krotkov, N., Yang, E.-S., Lamsal, L., Joiner, J., Castellanos, P., et al. (2021). Explicit and consistent aerosol correction for visible wavelength satellite cloud and nitrogen dioxide retrievals based on optical properties from a global aerosol analysis. *Atmospheric Measurement Techniques*, 14(4), 2857–2871. <https://doi.org/10.5194/amt-14-2857-2021>
- Vasilkov, A., Qin, W., Krotkov, N., Lamsal, L., Spurr, R., Haffner, D., et al. (2017). Accounting for the effects of surface BRDF on satellite cloud and trace-gas retrievals: A new approach based on geometry-dependent Lambertian equivalent reflectivity applied to OMI algorithms. *Atmospheric Measurement Techniques*, 10(1), 333–349. <https://doi.org/10.5194/amt-10-333-2017>
- Vasilkov, A., Yang, E.-S., Marchenko, S., Qin, W., Lamsal, L., Joiner, J., et al. (2018). A cloud algorithm based on the O<sub>2</sub>-O<sub>2</sub> 477 nm absorption band featuring an advanced spectral fitting method and the use of surface geometry-dependent Lambertian-equivalent reflectivity. *Atmospheric Measurement Techniques*, 11(7), 4093–4107. <https://doi.org/10.5194/amt-11-4093-2018>
- Veeffkind, J. P., Aben, I., McMullan, K., Förster, H., De Vries, J., Otter, G., et al. (2012). TROPOMI on the ESA Sentinel-5 Precursor: A GMES mission for global observations of the atmospheric composition for climate, air quality and ozone layer applications. *Remote Sensing of Environment*, 120, 70–83. <https://doi.org/10.1016/j.rse.2011.09.027>
- Veeffkind, J. P., De Haan, J. F., Sneep, M., & Levelt, P. F. (2016). Improvements to the OMI O<sub>2</sub>-O<sub>2</sub> operational cloud algorithm and comparisons with ground-based radar-lidar observations. *Atmospheric Measurement Techniques*, 9(12), 6035–6049. <https://doi.org/10.5194/amt-9-6035-2016>
- Voors, R., Dobber, M., Dirksen, R., & Levelt, P. (2006). Method of calibration to correct for cloud-induced wavelength shifts in the Aura satellite's Ozone Monitoring Instrument. *Applied Optics*, 45(15), 3652–3658. <https://doi.org/10.1364/AO.45.003652>
- Zoogman, P., Liu, X., Suleiman, R. M., Pennington, W. F., Flittner, D. E., Al-Saadi, J. A., et al. (2017). Tropospheric emissions: Monitoring of pollution (TEMPO). *Journal of Quantitative Spectroscopy and Radiative Transfer*, 186, 17–39. <https://doi.org/10.1016/j.jqsrt.2016.05.008>
- Zuidema, P., & Evans, K. F. (1998). On the validity of the independent pixel approximation for boundary layer clouds observed during ASTEX. *Journal of Geophysical Research*, 103(D6), 6059–6074. <https://doi.org/10.1029/98JD00080>